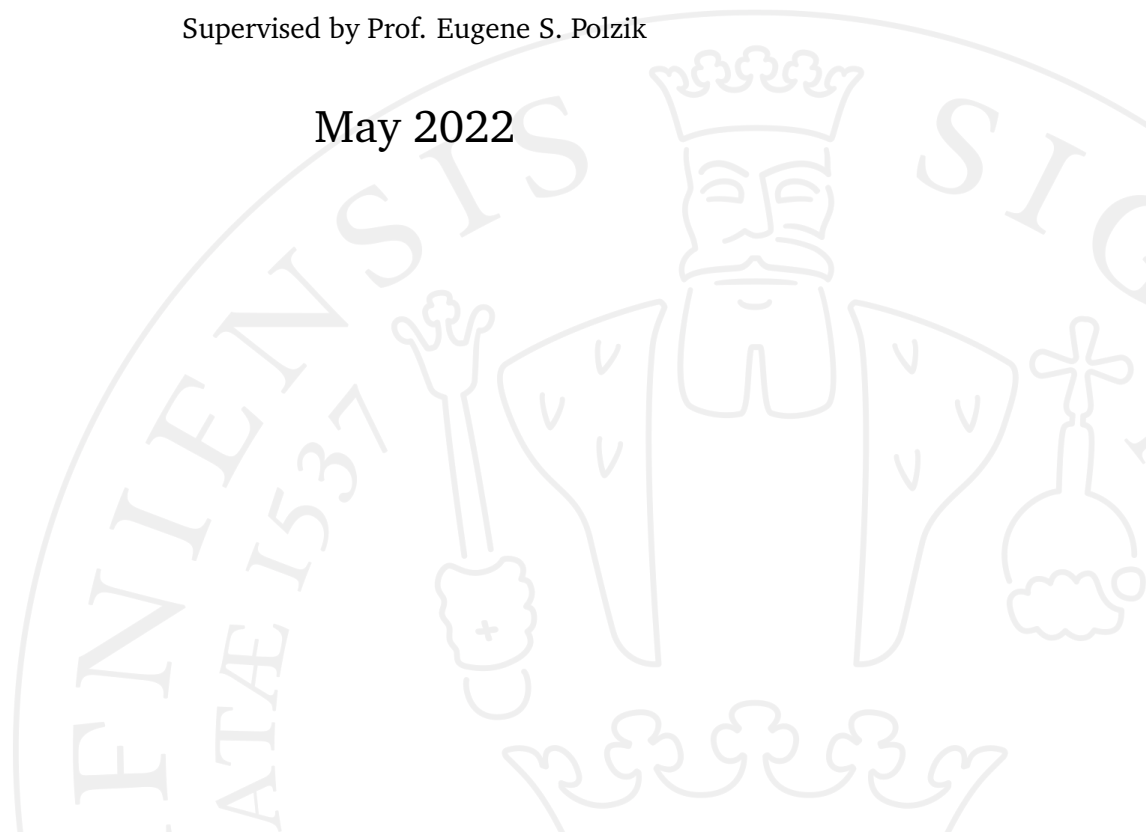**MSc in Physics**

Quantum Enhanced Optical Magnetic Induction Tomography through Back-Action Evasion and Conditional Spin Squeezing

Alan Oesterle

Supervised by Prof. Eugene S. Polzik

May 2022

Alan Oesterle

Quantum Enhanced Optical Magnetic Induction Tomography through Back-Action Evasion and Conditional Spin Squeezing

MSc in Physics, May 2022
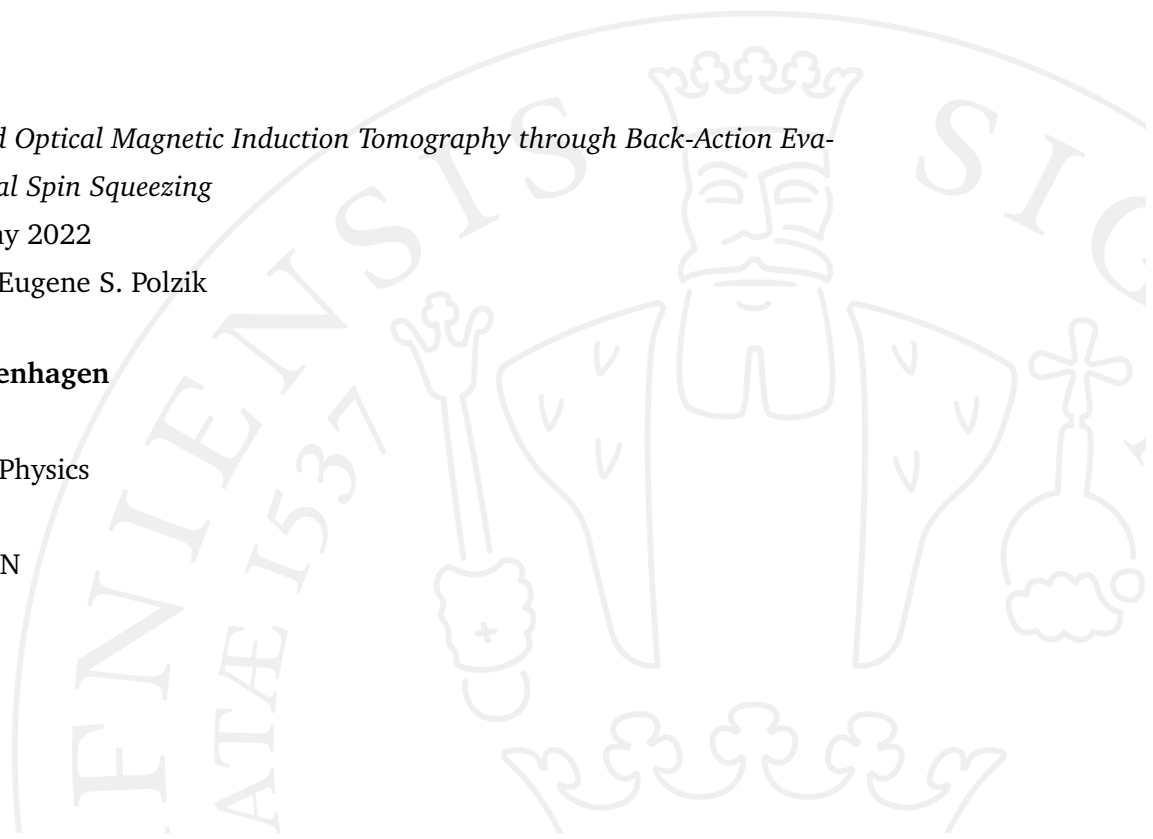
Supervisors: Prof. Eugene S. Polzik

University of Copenhagen

Niels Bohr Institut

Masters Degree in Physics

Blegdamsvej 17

2200 Copenhagen N

Acknowledgements

Abstract

Magnetic induction tomography (MIT) is a non-invasive method of detecting and imaging conductive objects. It is based on measuring the polarisation of light, sent through a cell filled with alkaline vapors, called optical magnetometers. It is a promising method, which can be used in various domains of science including medicine, for example the diagnostics of heart diseases. However the sensitivity of the magnetometry, and therefore MIT, is fundamentally restricted by the standard quantum limit (SQL), arising from the Heisenberg uncertainty principle. To exceed SQL, we applied stroboscopic back action evasion and conditional spin squeezing, achieving more than -4.6 ± 0.8 dB of squeezing at a Larmor frequency of 720kHz. By applying these techniques to our measurements of the MIT signal of a titanium sample, we were able to show a 73% increase in the signal to noise ratio.

Contents

Introduction

Magnetic Induction Tomography (MIT) is a non-invasive method of imaging the passive electromagnetic properties of an object. As MIT is a contact-less, non-invasive method it proves to be very helpful in several domains, such as bio-medicine or industrial process tomography. The basic principle behind MIT is to measure the magnetic field produced by eddy currents that are induced in an object. The magnetic field can be measured with different devices, the most common being an induction coil, as the coils have very high sensitivity at high frequencies[1]. Their sensitivity is, however, dependent on the operating frequency and it has been shown that for frequencies of lower than 50 MHz, the results are less than optimal. Alternatively superconducting quantum interference devices (SQUIDs) that can reach a sensitivity of 1 fT/$\sqrt{\text{Hz}}$ can be used [2]. However SQUIDs are expensive and more difficult to operate, due to the fact that they require cryogenic temperatures. Lately optical magnetometers have become more common. They use light to measure the response of an atomic ensemble of alkaline vapors contained in a glass cell to a magnetic field. It has been shown that they have the same sensitivity as SQUIDS[2].

The optical magnetometers can be further improved through quantum-enhanced metrology, which exploits quantum mechanical principles, specifically, entanglement and squeezing. Quantum-enhanced metrology has been demonstrated to improve the accuracy when time is measured with atomic clocks [3, 4, 5] and the sensitivity of gravitational-wave detection [6, 7, 8, 9]. For optical magnetometers, the SQL is set by the Heisenberg uncertainty of the spin projection and it sensitively scales with the number of atoms N as $1/\sqrt{N}$ [10].

Optical magnetometers are in use in a wide range of applications, and as they have high sensitivity and sub-millimeter resolution at room temperature [11], they are well suited to measure the weak magnetic fields of the human body for biomedical applications. Optical magnetometers were seen to detect brain activity [12, 13], heart beats [14] and nerve impulses [15]. One current major interest is in mapping the heart with MIT, where it could be utilized in the

diagnostic of cardiac arrhythmia (irregular heart beats) [16]. The images of the scar tissues on the heart combined with machine learning can be used to predict how likely a person is to have a heart attack [17].

In this project quantum-enhanced metrology is applied to improve the sensitivity and resolution of measurements beyond the standard quantum limit (SQL). To achieve this, an optical magnetometer- an anti-relaxation coated cesium vapor of micro cell size with a high spin lifetime - was utilized. Stroboscopic back-action evasion and conditional spin squeezing were employed to reduce the uncertainty. The MIT of a weakly magnetic titanium sample is presented as proof of concept, and to demonstrate the increase in the signal to noise ratio (SNR).

All of the experimental efforts presented in this thesis have been achieved from collaborative work and are in the manuscript in preparation: "Quantum enhanced electromagnetic induction measurement with an atomic magnetometer" [18].

Theory

2.1 Cesium

The optical magnetometers that are utilized in our lab require cesium atoms. Cesium is an alkaline metal and its chemical properties are primarily defined by its single valence electron. The energy of the valence electron is affected by the spin orbital interaction, a relativistic effect of the electron's intrinsic spin s coupling with its angular momentum l giving the total electronic angular momentum J. The energy of the electron is split further due to the coupling between the nuclear spin I and the total electronic angular momentum J, leading to the hyperfine structure defined by the total angular momentum F and it's sub-level m_F. This is shown in figure 2.1, where the hyper-fine splitting of the ground state and the first excited state can be seen. The nuclear spin of cesium 7/2 in the ground state ($l = 0$) has an electronic angular momentum of $J = 1/2$ and has a total angular momentum of either $F = 3$ or 4. We chose to denote the total angular momentum of a single atom by $\hat{j}$, because $\hat{J}$, not $\hat{F}$, is more commonly used in literature for spins.
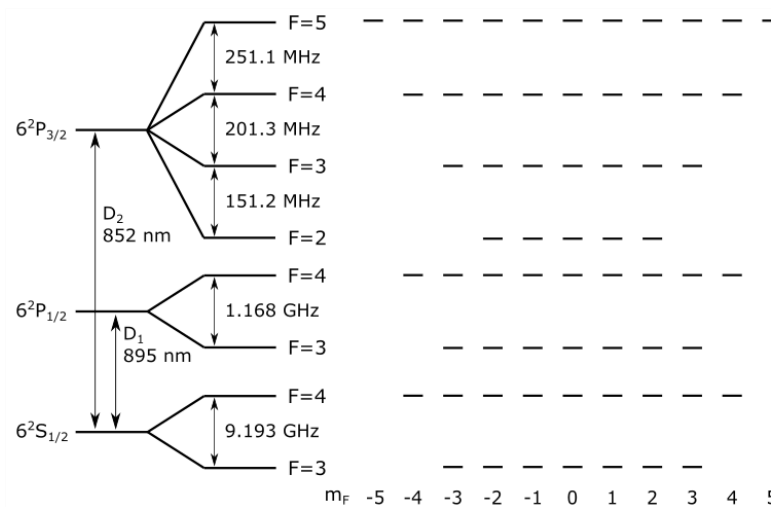

Figure 2.1.: The hyperfine splitting of the ground state and the first excited state [19]

The atomic system is composed of an ensemble of around 10^9 cesium atoms. The atomic state is described by the collective total angular momentum of the ensemble $\hat{J}$, which is the sum of the total angular momentum of the individual atoms $\hat{j}_i^n$

$$\hat{J}_i = \sum_{n=1}^{N} \hat{j}_i^n \tag{2.1}$$

with $i = x, y, z$, N is the number of atoms and n is the nth cesium atom in the atomic ensemble. The collective spin and the individual spins follow the commutation relation of angular momentum (with $\hbar = 1$)

$$\left[\hat{J}_i, \hat{J}_j\right] = i\epsilon_{ijk}\hat{J}_k \tag{2.2}$$

and have a Heisenberg uncertainty of

$$\text{Var}\left(\hat{J}_i\right)\text{Var}\left(\hat{J}_j\right) \geq \frac{\left\langle\hat{J}_k\right\rangle^2}{4} \tag{2.3}$$

Optical pumping is used to orient the spins in the system along the x-direction, moving the atoms into the F=4, $m_F = 4$ ground state, called the coherent spin state (CSS). In this state the minimal uncertainty is reached, $\text{Var}(\hat{J}_y) = \text{Var}(\hat{J}_z) = \frac{J_x}{2}$. The spin component along the x-direction is $J_x = N \cdot 4$, which is a large value and can be treated as a classic variable. The other two components $\hat{J}_y$ and $\hat{J}_z$ are small quantum variables that have Gaussian distributions with means of zero.

The large classical J_x enables two new quantum operators to be defined [20]

$$\hat{x} = \frac{\hat{J}_y}{\sqrt{J_x}} \quad \hat{p} = \frac{\hat{J}_z}{\sqrt{J_x}} \tag{2.4}$$

These operators are the canonical position $\hat{x}$ and momentum $\hat{p}$ operators. They are both continuous quantum operators when N is large.

The magnetic field Hamiltonian is $\hat{H}_b = \hbar\Omega\hat{J}_x$, where $\Omega = g_F\mu_B B/\hbar$ is the Larmor frequency, μ_B is the Bohr magneton and g_F is the Landé factor. The static magnetic field B causes the procession of $\hat{J}_y$ and $\hat{J}_z$ around the x-axis at

the Larmor frequency Ω. The transverse components can then be expressed in the rotating frame as [21]

$$\hat{J}'_y(t) = \hat{J}_y(t) \cos \Omega t + \hat{J}_z(t) \sin \Omega t \tag{2.5}$$

$$\hat{J}'_z(t) = \hat{J}_z(t) \cos \Omega t - \hat{J}_y(t) \sin \Omega t \tag{2.6}$$

where the operators marked with prime denote the rotating frame coordinates.

2.2 Light

The polarization states of light can be described by the Stokes operators, given by the differences of the number operators, $\hat{n}_{\mathrm{pol}}$, which give the number of photons polarized in different orthogonal bases [22]. The Stokes operators count the number of photons for a certain time duration and are dimensionless. For photons propagating in the z-direction these operators are

$$\hat{S}_x = \frac{1}{2}(\hat{n}_x - \hat{n}_y) \tag{2.7}$$

$$\hat{S}_y = \frac{1}{2}(\hat{n}_{+45°} - \hat{n}_{-45°}) \tag{2.8}$$

$$\hat{S}_z = \frac{1}{2}(\hat{n}_{+\sigma} - \hat{n}_{-\sigma}) \tag{2.9}$$

where $\hat{n}_x$ and $\hat{n}_y$ are the number operators for photons polarized in the x-direction and y-direction. Similarly, $\hat{n}_{\pm 45°}$ is the number of photons in the $\pm 45°$ direction and $\hat{n}_{\pm\sigma}$ for right or left handed circularly polarized photons. The Stokes operators follow the commutation relation of the angular momentum $\hat{J}$

$$[\hat{S}_i, \hat{S}_j] = i\epsilon_{ijk}\hat{S}_k \tag{2.10}$$

and have a Heisenberg uncertainty of

$$\mathrm{Var}(\hat{S}_i) \cdot \mathrm{Var}(\hat{S}_j) \geq \frac{\langle \hat{S}_k \rangle^2}{4} \tag{2.11}$$

When $\mathrm{Var}(\hat{S}_i) = \mathrm{Var}(\hat{S}_j) = \frac{1}{2}\langle \hat{S}_k \rangle$, the minimum uncertainty, is reached, light is said to be shot noise limited.

For a strong coherent x-linearly polarized light pulse, $\hat{S}_x$ can be treated as a classical value proportional to the photon flux, ϕ. The other two Stokes operators are quantum operators and have means of zero as there is an equal probability of ± 45 and $\pm \sigma$ polarization in x-polarized light. Similar to the atoms, the canonical operators of light can be defined as [23]

$$\hat{y} = \frac{\hat{S}_y}{\sqrt{S_x}} \quad \hat{q} = \frac{\hat{S}_z}{\sqrt{S_x}} \tag{2.12}$$

For light that is strongly polarized in the y-direction, $\hat{y}$ and $\hat{q}$ will be the quadratures of the x-polarized mode.

Experimentally, a lock-in amplifier was used to measure the light, as explained in section 3.1, and the signal is demodulated with a certain frequency. It is then important to look at the sine and cosine modes of the light operators at Larmor frequency. The cosine modes are [22]

$$\hat{q}_c(z) = \sqrt{\frac{2}{T}} \int_0^T \hat{q}(z,t) \cos{(\Omega t)} dt \tag{2.13}$$

$$\hat{y}_c(z) = \sqrt{\frac{2}{T}} \int_0^T \hat{y}(z,t) \cos{(\Omega t)} dt \tag{2.14}$$

where T is the duration of the interaction between the atoms and light. Assuming that $T \gg 1/\Omega$, the sine modes, $\hat{q}_s$ and $\hat{y}_s$, are the same except with sine instead of cosine.

2.3 Light and Atom Interaction

The interaction between the atoms and light originates from the dipole interaction of the electric field $\hat{E}$ of the light and the dipole moment d of the atoms, which gives a Hamiltonian of

$$\hat{H} = d \cdot \hat{E} \tag{2.15}$$

The effective interaction Hamiltonian of only the atoms in the ground state can be derived, and the full derivation is shown in [20]. To give a summary of the derivation, the cross sectional area of the interaction is assumed to be much

greater than the wavelength λ of the light, such that a one dimensional theory is sufficient. If the light is detuned far enough from the atomic transitions, the excited states' populations are small, and adiabatic elimination of the excited levels can be applied. The effective interaction Hamiltonian is then

$$
\begin{aligned}
\hat{H}_{int}^{eff} = -\frac{\hbar c \gamma \lambda^2}{8A\Delta\pi} \int_0^L & (a_0 \phi(z,t) n_a + a_1 \hat{S}_z(z,t) \hat{j}_z(z,t) \\
& + a_2[\phi(z,t)\hat{j}_z^2(z,t) - \hat{S}_-(z,t)\hat{j}_+^2(z,t) - \hat{S}_+(z,t)\hat{j}_-^2(z,t)])\rho A dz
\end{aligned}
\tag{2.16}
$$

where $j_\pm = j_x \pm i j_y$ are the ladder operators, γ is the gyromagnetic ratio, λ is the wave length of the light, Δ is the detuning, c is the speed of light, ρ is the atomic density, L is the length of the cell and A is the cross section of the cell. The first term containing a_0 is the Stark shift, that all of the atoms have regardless of their state, and the shift is proportional to the photon flux. The second term indicates the Faraday rotation, which rotates the Stokes operators $\hat{S}$ as well as the atomic spin J around the x-axis proportional to $\hat{J}_z$ and $\hat{S}_z$ respectively. The final term is due to higher order couplings between the light and the atoms. The parameters a_0, a_1 and a_2 are a scalar, a vector and a tensor term respectively. They depend on the detuning Δ with respect to hyper-fine splitting of the excited state, so that at large enough detuning, a_2 will vanish while a_0 and a_1 will be 4 and 1, respectively [20].

2.3.1 Equations of Motion

Let's assume that the atoms are in a CSS in the x direction and that light is propagating along the z direction and is polarized in the x direction. To derive the equation of motions for this system, the effective interaction Hamilton is used (equation 2.16). For the spin operator, the Heisenberg equation can be rewritten as [20]

$$
\frac{\partial}{\partial t}\hat{j}(t,z) = \frac{1}{i\hbar}[\,\hat{j}(t,z), \hat{H}_{int}^{eff}]
\tag{2.17}
$$

and for large detuning Δ where $a_2 \to 0$, the equations of motion are

$$
\frac{\partial}{\partial t}\hat{j}_x(t,z) = \frac{c\gamma\lambda^2}{8\pi\Delta}a_1\hat{j}_y(t,z)\hat{S}_z(t,z)
\tag{2.18}
$$

$$
\frac{\partial}{\partial t}\hat{j}_y(t,z) = -\frac{c\gamma\lambda^2}{8\pi\Delta}a_1\hat{j}_x(t,z)\hat{S}_z(t,z)
\tag{2.19}
$$

$$\frac{\partial}{\partial t}\hat{j}_z(t, z) = 0 \tag{2.20}$$

The equations of motion for the Stokes operators can be similarly derived [21]. The Heisenberg equation can be written as

$$(\frac{\partial}{\partial t} + c\frac{\partial}{\partial z})\hat{S}(t, z) = \frac{1}{i\hbar}[\,\hat{S}(t, z), \hat{H}_{int}^{eff}] \tag{2.21}$$

The speed of light, c, is assumed to be infinite, which means that the $\frac{\partial}{\partial t}$ term can be neglected. The equations of motion for the light operators at large detuning are then

$$\frac{\partial}{\partial z}\hat{S}_x(t, z) = \frac{\gamma\rho\lambda^2}{8\pi\Delta}a_1\hat{S}_y(t, z)\hat{j}_z(t, z) \tag{2.22}$$

$$\frac{\partial}{\partial z}\hat{S}_y(t, z) = -\frac{\gamma\rho\lambda^2}{8\pi\Delta}a_1\hat{S}_x(t, z)\hat{j}_z(t, z) \tag{2.23}$$

$$\frac{\partial}{\partial z}\hat{S}_z(t, z) = 0 \tag{2.24}$$

To solve these equations the input/output operators are used, where $\hat{S}_i^{in}(t)$ is defined as $c\hat{S}_i(t, 0)$ and $\hat{S}_i^{out}(t)$ is defined as $c\hat{S}_i(t, L)$ having operator units of 1/s. The input/output operators are then

$$\hat{S}_x^{out}(t) = \hat{S}_x^{in}(t)\cos 2\theta_F - \hat{S}_y^{in}(t)\sin 2\theta_F \tag{2.25}$$

$$\hat{S}_y^{out}(t) = \hat{S}_x^{in}(t)\sin 2\theta_F + \hat{S}_y^{in}(t)\cos 2\theta_F \tag{2.26}$$

$$\hat{S}_z^{out}(t) = \hat{S}_z^{in}(t) \tag{2.27}$$

with

$$\theta_F = -\frac{a_1\gamma\lambda^2\rho L}{32\pi\Delta}\langle\hat{j}_z\rangle \tag{2.28}$$

The above equations show the Faraday effect, as the Stokes operators are rotated around the z-axis by the Faraday angle of $2\theta_F$, which is proportional to the mean value of the spin component $\hat{j}_z$ of a single atom along the direction of the propagation of light. For linearly polarized light, a rotation of the polarization by an angle of θ_F along the path of propagation will be caused.

In the experiment, $\hat{S}_x$ and $\hat{J}_x$ are large classical values and it is assumed that the angle of rotation is small, $\theta_F \ll 1°$, and that J_x and S_x are constant

for the duration of the interaction. The collective spin is defined as $\hat{J}_i(t) = \int_0^L \hat{j}_i(t, z)\rho A dz$, so that the equation of motion for the spin operators are

$$\frac{\partial}{\partial t} J_x(t) = 0 \tag{2.29}$$

$$\frac{\partial}{\partial t} \hat{J}_y(t) = a J_x \hat{S}_z^{in}(t) \tag{2.30}$$

$$\frac{\partial}{\partial t} \hat{J}_z(t) = 0 \tag{2.31}$$

with

$$a = -\frac{\gamma \lambda^2}{16\pi\Delta} a_1 \tag{2.32}$$

and the input/output equations for the Stokes operators are

$$S_x^{out}(t) = S_x^{in}(t) \tag{2.33}$$

$$\hat{S}_y^{out}(t) = \hat{S}_y^{in}(t) + a S_x^{in}(t)\hat{J}_z(t) \tag{2.34}$$

$$\hat{S}_z^{out}(t) = \hat{S}_z^{in}(t) \tag{2.35}$$

Equations 2.34-36 show the rotation of the polarization by an angle of a. This angle arises from the spin that is oriented along the direction of the propagation of light. When $\hat{S}_y^{out}(t)$ is measured, information about $\hat{J}_z(t)$ is acquired. When $\hat{J}_z(t)$ is conserved during the interaction, this is known as a quantum non-demolition (QND) measurement.

To insert the effect of the homogeneous magnetic field into the equations of motion, H_B was included in the Hamiltonian. The total angular momentum $\vec{J}$ is rotating around the magnetic field B at the Larmor frequency Ω. Then the rotating frame coordinates (eq 2.5 and eq 2.6) are used and the equations of motion transform into

$$\hat{S}_y^{out}(t) = \hat{S}_y^{in}(t) + a S_x^{in}(t)(\hat{J}_y'(t)\sin\Omega t + \hat{J}_z'(t)\cos\Omega t) \tag{2.36}$$

$$\hat{S}_z^{out}(t) = \hat{S}_z^{in}(t) \tag{2.37}$$

$$\frac{\partial}{\partial t} \hat{J}_y'(t) = a J_x \hat{S}_z^{in}(t)\cos\Omega t \tag{2.38}$$

$$\frac{\partial}{\partial t} \hat{J}_z'(t) = -a J_x \hat{S}_z^{in}(t)\sin\Omega t \tag{2.39}$$

As shown both $\hat{J}'_y$ and $\hat{J}'_z$ contribute to the $\hat{S}^{out}_y$ component after the interaction. We can also see that the time derivatives of the transverse spin components contain $\hat{S}_z$, the so called back action noise (BAN). BAN arises when the light is linearly polarized $\langle \hat{S}_z \rangle = 0$ and comprises only noise, which is imprinted on $\hat{J}'_y$ and $\hat{J}'_z$ and thereafter is fed back into the measurement of $\hat{S}^{out}_y$.

2.3.2 Coupling Strength

The coupling strength of the light-atom interaction is denoted as $\kappa^2 = a^2 S_x J_x T$, where T is the duration of the interaction, and an important parameter for comparing the different quantum noises in stroboscopic spin squeezing [21]. The coupling strength is proportional to the number of atoms and photons. It is a dimensionless constant, which can be derived from the input/output equations 2.36- 2.39. The following equations show the rewritten input/output equations with the canonical variables of light and atoms

$$\hat{y}^{out}(t) = \hat{y}^{in}(t) + a\sqrt{S_x J_x}(\hat{x}(t)\sin\Omega t + \hat{p}(t)\cos\Omega t) \tag{2.40}$$

$$\hat{q}^{out}(t) = \hat{q}^{in}(t) \tag{2.41}$$

$$\frac{\partial}{\partial t}\hat{x}(t) = a\sqrt{S_x J_x}\hat{q}^{in}(t)\cos\Omega t \tag{2.42}$$

$$\frac{\partial}{\partial t}\hat{p}(t) = -a\sqrt{S_x J_x}\hat{q}^{in}(t)\sin\Omega t \tag{2.43}$$

As $\hat{q}^{in}(t)$ is unchanged during the interaction, equations 2.43 and 2.42 can be rewritten as

$$\hat{x}(t) = \hat{x}^{in} + \int_0^{t'} a\sqrt{S_x J_x}\hat{q}^{in}(t')\cos\Omega t' \, dt' \tag{2.44}$$

$$\hat{p}(t) = \hat{p}^{in} + \int_0^{t'} a\sqrt{S_x J_x}\hat{q}^{in}(t')\sin\Omega t' \, dt' \tag{2.45}$$

which can be used to calculate the sine and cosine modes of $\hat{y}^{out}$ integrated over an interaction time T. The following equations show the measured variables of the experiment by the lock-in amplifier.

$$\hat{y}_c^{out} = \sqrt{\frac{2}{T}} \int_0^T \hat{y} \cos(\Omega t) dt$$

$$= \hat{y}_c^{in} + \frac{\kappa}{\sqrt{2}} \hat{p}^{in} - \kappa^2 \sqrt{\frac{2}{T^3}} \int_0^T \cos^2(\Omega t) dt \int_0^{t'} \hat{q}^{in}(t') \sin(\Omega t') dt' \qquad (2.46)$$

$$\approx \hat{y}_c^{in} + \frac{\kappa}{\sqrt{2}} \hat{p}^{in} - \kappa^2 \sqrt{\frac{2}{T^3}} \int_0^T \frac{(T-t)}{2} \hat{q}^{in}(t) \sin(\Omega t) dt$$

As it is assumed that the interaction duration T is much lager than $1/\Omega$ and that the evolution of the system is slower than $1/\Omega$, the term with $\cos(\Omega t) \sin(\Omega t)$ is ignored. Similarly for the sine mode

$$\hat{y}_s^{out} \approx \hat{y}_s^{in} + \frac{\kappa}{\sqrt{2}} \hat{x}^{in} - \kappa^2 \sqrt{\frac{2}{T^3}} \int_0^T \frac{(T-t)}{2} \hat{q}^{in}(t) \cos(\Omega t) dt \qquad (2.47)$$
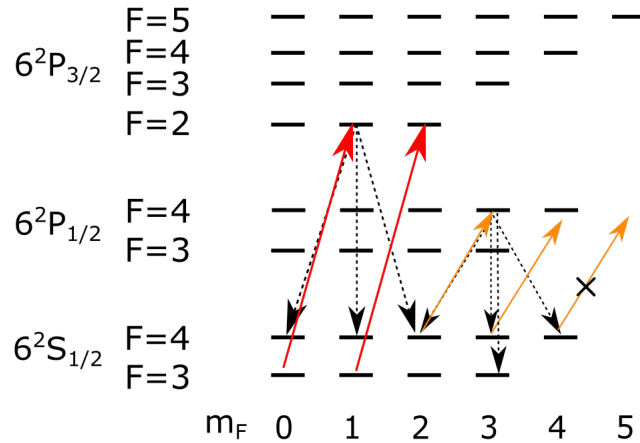
2.4 Optical Pumping

Figure 2.2.: Depicting the principals of optical pumping, the effect of the circularly polarized pump and repump laser are depicted by the orange and red arrows, respectively [19]

A large number of atoms are in the system. Therefore it is desirable to have all of the atoms in the same spin state and for that spin state to have a large spin since the signal scales with the spin. This signifies the $F=4$, $m_F=4$ state for

cesium atoms. At room temperature, all levels of the ground state hyper-fine manifolds are equally populated. A pumping scheme is used to prepare the atoms in the ensemble for the desired state. The atoms are excited to such a high energy state that they absorb a photon. Since the momentum of the photon has to be conserved, only certain transitions are allowed. The selection rules are [24]

$$\begin{aligned}
\Delta l &= \pm 1 \\
\Delta s &= 0 \\
\Delta j &= 0, \pm 1 \\
\Delta F &= 0, \pm 1
\end{aligned} \qquad (2.48)$$

and depending on the polarization of the photon the allowed transition of the hype-fine Zeeman sub-states are

$$\begin{aligned}
\pi &\to \Delta m_F = 0 \\
\sigma_+ &\to \Delta m_F = +1 \\
\sigma_- &\to \Delta m_F = -1
\end{aligned} \qquad (2.49)$$

where π denotes linearly polarized light along the x-direction and $\sigma_\pm$ denotes right/left circularly polarized light. The atoms will return to the ground state by spontaneous emission with the selection rule $\Delta m_F = 0, \pm 1$ The optical pumping scheme is shown in figure 2.2 and is achieved by the employment of two lasers.

The pump laser is right circularly polarized, σ_+, and set to resonate to the $F = 4$ to $F' = 4$, 895nm D_1 transition. When an atom absorbs a photon from this laser, the atom's angular momentum is increased, ($\Delta m_F = +1$), and when it decays to the ground state by spontaneous emission, the atom emits a randomly polarized photon and on average moves up one m_F level. The atom will keep moving up until it reaches $m_F = 4$ state. $m_F = 4$ is a dark state where there is no allowed transition with σ_+ polarized photons.

The repump laser is also right circularly polarized, σ_+, and is set to resonate to the $F = 4$ to $F' = 2, 3$, 852nm D_2 transition. Its purpose is to empty the $F=3$ ground state by exciting the atoms, which then decay to either the $F=4$ or 3 ground state by spontaneous emission. Depending on the strength of the repump laser, a percentage of the atoms will be in the $F=3$ state and not contribute to the collective spin state as they do not interact with the probe.

Experimental Details

3.1 General Setup
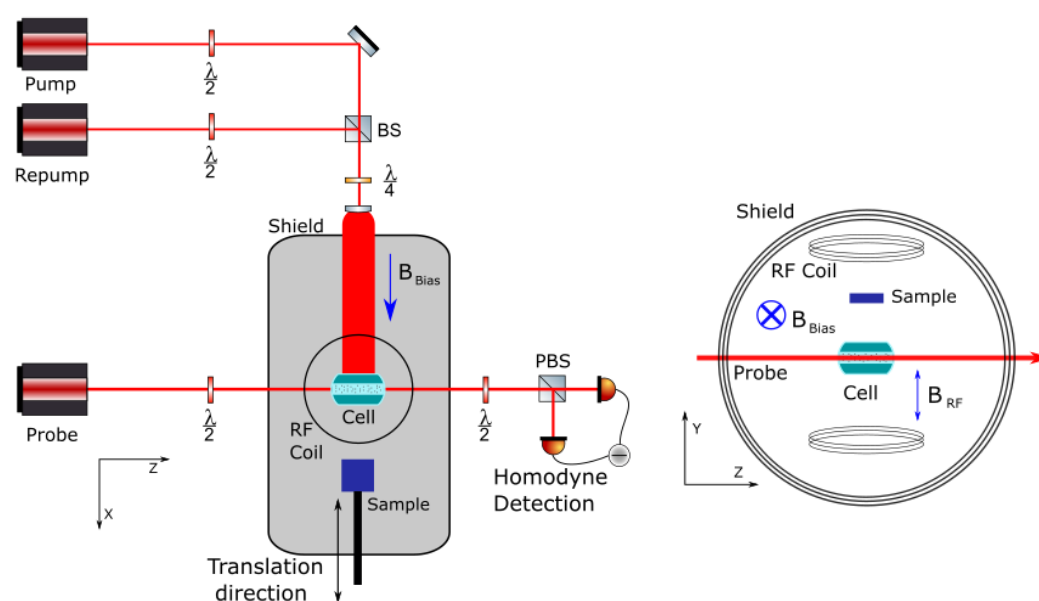
(a) Conceptual schematic of the setup, depicting the pump, repump and probe path, cell, sample, bias magnetic field orientation, the wave plates, beamsplitter and polarizing beamsplitter, and the half and quarter wave plat, denoted as $\lambda/2$ and $\lambda/4$ respectively

(b) The arrangement of the RF coil, sample, cell, prob path, and bias magnetic field inside the shield

Figure 3.1.: Experimental setup

The simplified experimental system is shown in figure 3.1 along with a vertical cross section of inside the shield. Three lasers were used in the experiment: The probe, pump and repump lasers. The pump and repump lasers were combined with a 50/50 beamsplitter (BS). The beam then passed through an achromatic quarter wave plate to circularly polarize the light. A pair of lenses were used to horizontally widen the waist of the beam, as to have the laser shine through out the entire length of the cell. After the probe beam passed through the cell, it traveled through a half wave plate and a polarizing beamsplitter (PBS). The two beams were measured with photodiodes and the difference of the two photo currents was measured. The half wave plate

shifted the direction of the polarization of the probe and was set to an angle so that the signal measured is proportional to $\hat{S}_y^{out}$. $\hat{S}_y^{out}$ was then measured as it contains information about the $\hat{J}_z$ (eq. 2.39), and the wave plate is set correctly when the measured current is zero as $\langle \hat{S}_y^{out} \rangle = 0$ when $\langle \hat{J}_z \rangle = 0$. The detection of the signal is similar to a balanced homodyne detection, where the strong local oscillator is the y-polarized coherent light and the weak quantum field is the x-polarized part.

The measured voltage was then sent into a lock-in amplifier (LIA) to extract the strength of the signal of a chosen frequency. The LIA works by multiplying the input signal with a reference signal and by integrating it over a period much smaller than the measurement time, demodulating the information carried at the reference signal. The reference signal is set to the Larmor frequency and has a specific phase that can be set by the LIA. The LIA gives out two components, one that is in phase with the reference signal and one that is 90° out of phase. These two components correspond to the sine and cosine components of the input signal.
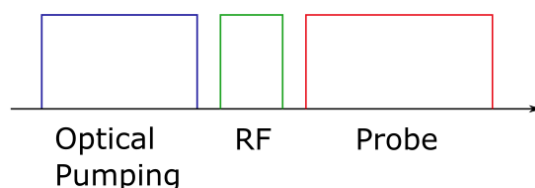

Figure 3.2.: The pulse sequence used to characterizes the atomic ensemble

The experiment was done in pulse mode. Many different pulse sequences were used for the experiment. The pulse sequence shown in figure 3.2 was used to characterize the atomic ensemble. The optical pumping was used to initialize the atoms in the CSS. A RF pulse at the Larmor frequency was applied to give the atomic ensemble a transverse component to the spin, and then the atomic ensemble was probed. The experiment was done in pulse mode because the decoherence time in pulse mode is longer than the decoherence time in a continuous wave mode (the lasers are on all the time), since the decay rate in the dark is much smaller. Each laser travels through an acousto-optic modulator (AOM). The AOMs were carried out with a 80MHz modulation and the first order of diffraction was used for the experiment. The lasers can then be turned off by switching off the modulation, leading to the pulse sequence being controlled by a function generator. The sharp edges of the pulses include the high frequency components which would introduce extra noise in the

measurement. Therefore the shape of the pulse for the pump and repump were changed to have soft edges.
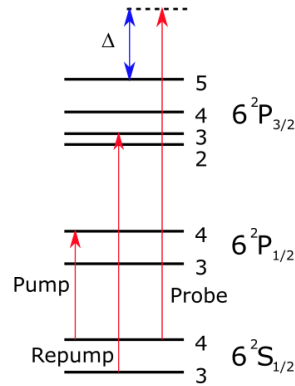
3.1.1 The Laser System

Figure 3.3.: Level scheme of the cesium with the pump, repump, and probe laser transitions used

The lasers are TOPTICA external cavity diode lasers. The pump and repump lasers are locked at the 895nm, $F = 4$ to $F' = 4$ on D_1 and the 852nm, $F = 4$ to $F' = 2, 3$ on D_2 transitions, respectively. whereas the probe is locked at a frequency that is far detuned from the D_2 transition. To lock the pump and repump lasers at a desired frequency, a small percentage of the output of the laser is split off and travels through a cesium vapor cell, where Doppler-free (saturated) absorption spectroscopy is used to resolve the peaks for the different transitions. There are some additional (crossover) peaks in the spectrum, which are an effect of the counter-propagating beams used in Doppler-free (saturated) absorption spectroscopy. Crossover peaks are formed when an atom is on resonance to one transition with one beam and on resonance to the neighboring transition with the other beam. Between those two transitions a peak will form. To lock the frequency at the desired peak, a feedback system that utilizes the derivative of the spectrum is used. This is called the error signal [25].

As for the probe, the error signal first travels through an electro-optical modulator (EOM) and is then locked using a similar setup. The EOM is used to generate side bands of around 900 MHz. The second side band is selected to blue detune the probe laser by 1.9GHz from the $F' = 4, 5$ cross peak. The $F = 4$ to $F' = 4, 5$ cross peak is selected when locking the laser.

3.1.2 The Atomic Vapor Micro Cells

Figure 3.4.: Picture of cell

Cesium atoms are inside a paraffin coated glass micro cell, as shown in figure 3.4. The micro cell is a glass chip that is encapsulated by a glass cylinder with a stem that contains solid cesium. The glass chip has a long micro channel that is $2.5\,\mathrm{cm}$ long and has a $500\,\mu\mathrm{m}$ by $500\,\mu\mathrm{m}$ cross section. The cesium vapor pressure is determined by the temperature of the cell, there is in order of 10^9 of cesium atoms in the cell at room temperature. The velocity of the atoms at room temperature have a Maxwell-Boltzmann distribution with a average thermal velocity of [26]

$$\bar{v} = \sqrt{\frac{8k_B T}{\pi m_{\mathrm{Cs}}}} \approx 219\mathrm{m/s} \tag{3.1}$$

where k_B is the Boltzmann constant, T is the temperature and m_{Cs} is the mass of a Cesium atom. The time in between wall collisions for an atom is $T_{wall} = 4V/\bar{v}A = 2.3\mu s$, where V and A are the cell volume and surface area respectively, leading to around 440 collisions per millisecond with the glass walls. When an atom collides with the glass wall, it is absorbed into the surface of the glass for a short amount of time (in the order of a microsecond). When it is ejected back out, the atom's spin orientation will be random as it interacted with the local electromagnetic field of the glass [26]. There are two common methods to suppress this effect. One of them is to apply an anti-relaxation surface coating on the walls of the cell. This would allow the atoms to bounce off the surface many times without losing their spin orientation. The other method is to fill the cell with a buffer gas to slow the cesium atoms diffusion, increasing the time it takes to get to the wall. They both have their respective advantages and disadvantages. For our experiment, cells with anti-relaxation surface coating are used.

The thermal motion of the atoms has some advantages as some of the conditions are inhomogeneous in the cell and the motion of the atoms creates an averaging effect, called thermal averaging. The probe beam does not fill the entire cell with the same intensity as its beam width is slightly smaller than the width of the cell and is Gaussian distributed. The atoms move in and out of the probe beam many times during the measurement and on average they have the interaction strength. The inhomogeneity of the magnetic field causes the atoms to have different Larmor frequencies and similarly the motion of the atoms will make it, that on average they have the same Larmor frequency.

3.1.3 Magnetic field and The Magnetic shield

Figure 3.5.: A picture of the magnetic shield

To protect the cesium atoms from stray magnetic fields, the cell is placed inside a magnetic shield as shown in figure 3.5. The magnetic shield is a cylinder made up of layers of iron, mu-metal and aluminum. The iron and mu-metal layers have high magnetic permeability, which allows the shield to better conduct magnetic fields[24]. The shield alters the path of stray magnetic fields, such that the fields travel around rather than through the shield. The aluminum layer is to shield for any fast oscillating magnetic fields, as it acts as a sort of Faraday cage. The shield has some holes cut in the sides, firstly to allow the lasers to pass through, and secondly for the cell to be mounted. There is a coil system around the aluminum layer to generate a constant bias magnetic field B_{Bias} in the cell. The coil system is made of three different coil subsystems, the first one is the main coil, which generates the main magnetic field inside the shield. The other two coils are the compensation coil and the saddle coil, which are used to compensate for the magnetic field inhomogeneity of the main coil. A high resistance wire is also part of the system in order to heat the cell, to avoid generating a magnetic field, the wire is twisted around itself.

A pair of RF coils is placed inside the aluminum layer to generate an RF magnetic field B_{RF}. The first coil, placed closer to the sample, is there to induce eddy currents in the sample to generate a secondary magnetic field. The other coil is there to remove the signal and the noise form the first coil. If there was only one RF coil, the total signal measured would come from both the primary magnetic field plus the secondary magnetic field. The main issues with this setup is that the noise is proportional to the amplitude of the signal. The second coil is used to generate a magnetic field such that the total magnetic field of the two coils along the cell is zero and that the only signal measured comes from the secondary field [27].

3.2 Spin Life Time

The life time of the CSS is characterized by two decay constants, T_1 and T_2[22]. T_1 is the decay constant of the mean spin $\langle J_x(t) \rangle = \langle J_x(0) \rangle e^{-t/T_1}$. The decay of the mean spin is due to population transfer into the different Zeeman sublevels of the $F=4$ ground state or to the $F=3$ ground state. The decay time in the dark is slower than when a laser is on, due to spontaneous emission. When an atom moves to the the $F=4$, $m_F = 3$ or 2 states, it will still contribute to the mean spin, but its contribution will be reduced by a factor of $\frac{3}{4}$ or $\frac{1}{2}$ (equation 2.1) respectively. On the other hand if the atom moves to the $F=3$ state, it will not contribute to the mean spin as it does not interact with the probe.

T_2 is the decay constant for the transverse spin $\langle J_\perp(t) \rangle = \langle J_\perp(0) \rangle e^{-t/T_2}$. T_2 is usually much smaller than T_1, as it is affected by phase fluctuations along with the same decay mechanisms of T_1. As shown in [22] and [21], the decay rate $\Gamma = 1/(\pi T_2)$ can be parameterized as

$$\Gamma = a + b\theta_F + c\text{P} + d\text{P}^2 + e\theta_F\text{P} \qquad (3.2)$$

The first term of the equation 3.2, a, symbolizes the decay caused by wall collisions, atoms leaving the effective cell volume, and the magnetic field instabilities. The second term is proportional to the Faraday angle and stands for the atom-atom collisions. Both terms constitute the decay rate in the dark. The third term, proportional to the probe power P corresponds to the spontaneous emission caused by the probe. The term quadratically proportional to the

probe power means the inhomogeneous intensity distribution of the probe that causes the atoms to experience different Stark shifts leading to dephasing of the atoms. The last term comes from higher order coherent interaction between light and atoms.

3.3 Atomic state characterization, MORS

The model describing the light atom interaction is reliant on the atoms being in the CSS, hence it is important to verify how well prepared the atomic ensemble is in that state. An RF magnetic field is used to excite coherent transitions between the different magnetic sub-levels in order to measure the orientation of the atomic ensemble[20]. According to equation 3.6, the transverse spins are modulated by these coherence transitions and then measured by the probe light. This process is called the Magneto-Optical Resonance Signal (MORS).

For a system with N atoms in the hyperfine F=4 ground state, the spin state density operators are defined as [20]

$$\hat{\sigma}_{ij} = \frac{1}{N} \sum_{n=1}^{N} \hat{\sigma}_{ij}^{n} = \frac{1}{N} \sum_{k=1}^{N} |i\rangle_n \langle j|_n \tag{3.3}$$

with i, j = -F, -F+1, ..., F and $|i\rangle_n$ referring to the nth atom in the magnetic sub-level m_F= i. The macroscopic atomic spin of the atoms in the F=4 ground state can also be expressed in terms of the density operators

$$\hat{J}_x = N \sum_{m=-F}^{F} m\hat{\sigma}_{mm} \tag{3.4}$$

$$\hat{J}_y = N \sum_{m=-F}^{F-1} \sqrt{F(F+1) - m(m+1)}(\hat{\sigma}_{m+1,m} + \hat{\sigma}_{m,m+1}) \tag{3.5}$$

$$\hat{J}_z = N \sum_{m=-F}^{F-1} i\sqrt{F(F+1) - m(m+1)}(\hat{\sigma}_{m+1,m} - \hat{\sigma}_{m,m+1}) \tag{3.6}$$

where the x axis is the quantization axis. For MORS measurements, the atoms are placed in an external constant magnetic field B, that causes a shift in the energy of the magnetic sub-levels as shown in figure 3.6. An RF magnetic field perpendicular to the macroscopic one is applied. This field induces $\Delta m = \pm 1$ transitions between the magnetic sub-levels when the frequency is
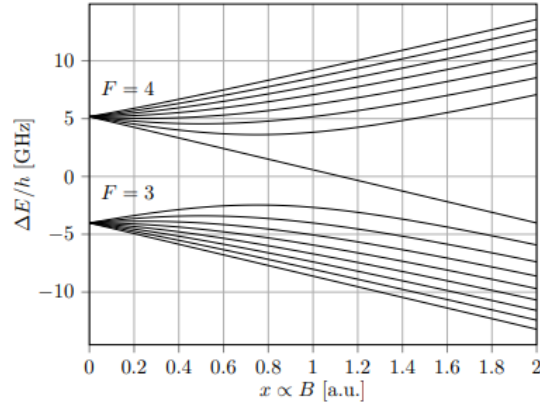
Figure 3.6.: The Zeeman splitting for all ground state hyperfine sub-levels due to an external magnetic field [28]

on resonance with the level splitting. The interaction of the atoms with the magnetic fields is described with the Hamiltonian

$$\hat{H}_{mag} = g_F \mu_B \vec{J} \cdot \vec{B} + O(B^2) \tag{3.7}$$

where μ_B is the Bohr magneton and g_F is the Landé factor[21]. The second term in the equation describes the higher order effect. This higher order effect contains the quadratic Zeeman effect, which is of importance to the experiment as it is preformed in the intermediate non-linear regime. The quadratic Zeeman effect creates a splitting between the magnetic sub-levels of $\upsilon_{qz} = 2\Omega/\upsilon_{hfs}$, where $\upsilon_{hfs} = 9.1926$GHz is the hyperfine splitting of the cesium ground state[21]. The time derivatives from the transverse spin components with the RF field in the rotating frame are

$$\frac{\partial}{\partial t}\hat{J}_y'(t) = \omega J_x \cos{(\Omega t)} \cos{((\Omega_{RF} t)}, \quad \frac{\partial}{\partial t}\hat{J}_z'(t) = -\omega J_x \sin{(\Omega t)} \sin{(\Omega_{RF} t)} \tag{3.8}$$

where $\omega = g_F u_B B_{RF}/\hbar$ and B_{RF} is the amplitude of the RF magnetic field. When the RF field is on resonance, $\Omega_{RF} = \Omega$ and the time scale of the interaction is long in comparison to the oscillations, the equations can be rewritten as $\frac{\partial}{\partial t}\hat{J}_y'(t) = \frac{\partial}{\partial t}\hat{J}_z'(t) = \frac{\omega J_x}{2}$. The RF field creates a displacement in the rotating spin when it is on resonance with one of the $\Delta m = \pm 1$ coherence. The sine and cosine components of $\hat{S}_y^{out}$ are measured with a lock-in amplifier, which is

set to give the sum of the squared of the amplitude of the two components. The amplifier then gives the MORS signal, which is proportional to

$$\text{MORS}(\omega) \propto | \sum_{m=-F}^{F-1} \frac{F(F+1) - m(m+1)}{i(\Omega_{m,m+1} - \omega - \Gamma_{m,m+1}/2)} e^{i\Omega_{RF}} [\sigma_{m+1,m+1} - \sigma_{m,m}] |^2$$

(3.9)

with $\Gamma_{m,m+1}$ the transverse spin decay rates and $\Omega_{m,m+1}$ the coherent frequencies of the individual levels. The results are shown in figure 3.7, where the quadratic Zeeman splitting of 460 Hz shows eight Lorentzian peaks for partially polarized 60% states (figure 3.7a) and only two peaks can be seen for a highly polarized 90% state (figure 3.7b). The polarization, p, is defined as [20]

$$p = \frac{1}{F} \sum_{m=-F}^{F} m \cdot \langle \sigma_{m,m} \rangle$$

(3.10)

where F=4 and $\langle \sigma_{m,m} \rangle$ are the population of the different magnetic sub-levels in F=4, under the condition that the sum of all of the populations is equal to one, $\sum_{m=-F}^{F} \langle \sigma_{m,m} \rangle = 1$. If all of the atoms were in the m=4 sub-level then p=1, however if the sample was unpolarized then p=0.

To calculate the polarization from the results shown in figure 3.7, the data needs to be fitted. The MORS measurements were done at the Larmor frequency of 1.46 MHz, as the quadratic Zeeman splitting for 720 kHz is not well resolved. The splitting is 210 Hz and the peak line width is 120 Hz. The polarization is calculated at 1.46 MHz and it is assumed to be the same at 720 kHz. There are two methods that are used to calculate the polarization. The first is described in [20], where there is only one parameter for the height of the peaks and the populations of the different sub-levels are assumed to have an exponential decay, $\langle \sigma_{m,m} \rangle = \langle \sigma_{4,4} \rangle \epsilon^{4-m}$, where $\epsilon = e^{\beta}$ is a function of p. This method works well for highly polarized states, however for partially polarized states with large quadratic Zeeman splitting, the polarisation is overestimated. The second method is by having each peak height as a parameter when fitting, The peak height is proportional to the difference in population of the two neighboring sub-levels [22, 29]. The polarization is then calculated, using the fact that the sum of all of the populations must be equal to one and with the assumption that the m=-4 sub-level is empty.
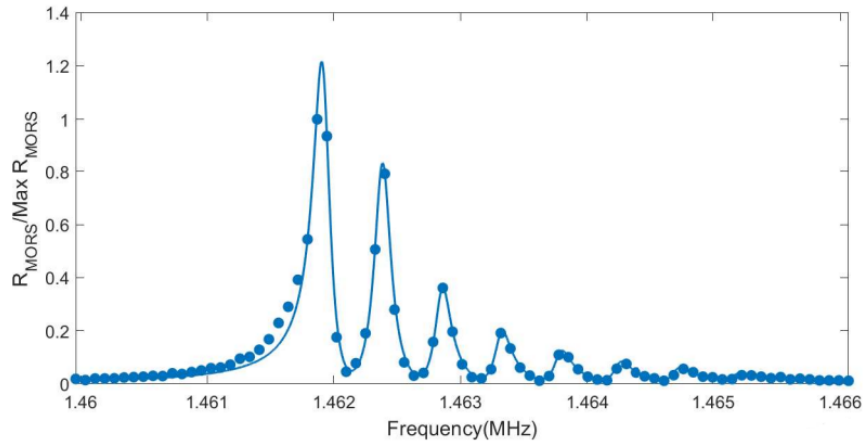
(a) Pump power$=0\ \mu W$
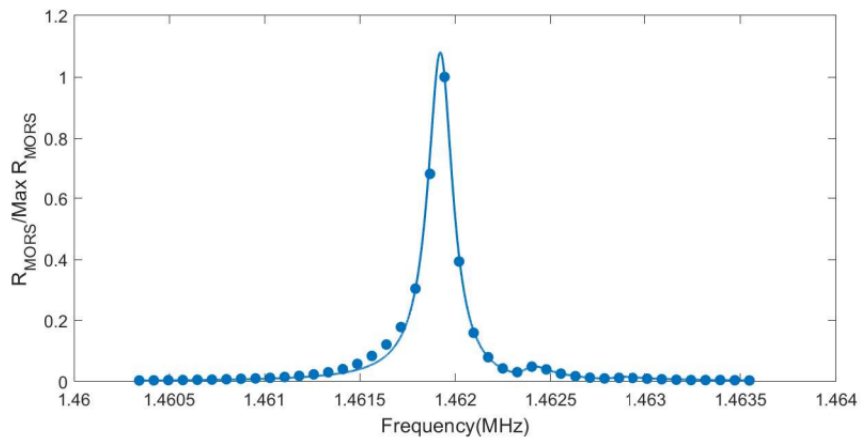
(b) Pump power$=200\ \mu W$

Figure 3.7.: MORS signal at a Larmor frequency of 1.46 MHz for a partially polarized state (a) and for a highly polarized state (b)

3.4 Quantum Noise

The precision of the measurements is fundamentally limited by quantum fluctuations. Quantum noise can come from the shot noise of the probe laser, spin projection noise from the atomic ensemble and is back-action noise. The noise measurements are done by measuring 1600 times the average of the demodulated time-signal that is acquired. The noise is then the variance of the 1600 averages.

3.4.1 Light noise

The noise of the incoming light is called the photon shot noise (SN). For light in a CSS, it was shown in equation 2.11 that the noise of the light with number n_{ph} of photons is [22]

$$\text{Var}(\hat{S}_y) = \text{Var}(\hat{S}_z) = \frac{\langle \hat{S}_x \rangle}{2} = \frac{n_{ph}}{2} \tag{3.11}$$

The shot noise is a white spectrum noise and is proportional to the photon number. The SN is used to scale the other types of noise in the system as spin squeezing will be applied in later measurements to reduce the noise. The SN is not reduced during spin squeezing and if it is too large, it will dominate over the other quantum noises. If the measurement is limited by quantum fluctuations, the SN should scale linearly with probe power. Any classical noise in the system will contribute a quadratic component to the scaling.

To measure the SN, the main magnetic field is changed significantly, such that the Larmor frequency is a few line-width away from the LIA bandwidth. As the SN is a white spectrum noise, it should not be affected when the magnetic field is changed back for the other measurements. Any signal from the atomic spin in the measurement is filtered out by the LIA. The SN is calculated by subtracting the electronic noise from the variance of the measurement.

$$SN = \sigma^2_{measured} - EN \tag{3.12}$$

The electrical noise (EN) is the noise from the electrical components in the setup and is measured by recording the signal when all of the light is blocked. The SN is shown in figure 3.8 and it scales linearly with the number of photons, demonstrating that the light is SN limited.

3.4.2 Atomic noise

As the atomic observable cannot be measured directly, the light atom interaction (section 2.3) is used to do quantum state tomography in order to reconstruct the atomic noise [22]. The information of the atomic state is mapped onto the light and from the measurement of the light, the mean
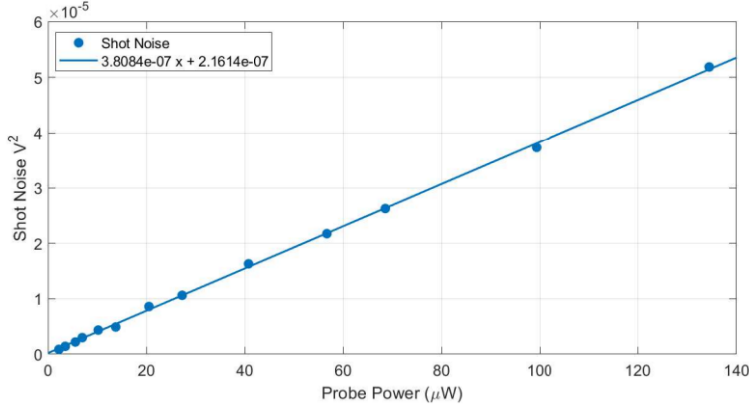
Figure 3.8.: The photon shot noise versus the probe power

and variance of the atomic state can be reconstructed using the input/output equations.

In the case of QND measurements, the variances of the measured light observable can be given as [21]

$$\text{Var}(\hat{y_c^{out}}) = \text{Var}(\hat{y}_c^{in}) + \frac{\kappa^2}{2}\text{Var}(\hat{p}^{in}) + \frac{\kappa^4}{12}\text{Var}(\hat{q}^{in}) \tag{3.13}$$

$$\text{Var}(\hat{y_s^{out}}) = \text{Var}(\hat{y}_s^{in}) + \frac{\kappa^2}{2}\text{Var}(\hat{x}^{in}) + \frac{\kappa^4}{12}\text{Var}(\hat{q}^{in}) \tag{3.14}$$

For a system prepared in the CSS, the uncertainty would be $\text{Var}(\hat{p}^{in}) = \text{Var}(\hat{x}^{in}) = \frac{1}{2}$ and if the light is shot noise limited $\text{Var}(\hat{y_s^{in}}) = \text{Var}(\hat{q}^{in}) = \frac{1}{2}$. Consequently the above equation can then be written as

$$\text{Var}(\hat{y_{c/s}^{out}}) = \frac{1}{2}(1 + \frac{\kappa^2}{2} + \frac{\kappa^4}{12}) \tag{3.15}$$

The first term of the equation is the SN of the light, the second term is the spin projection noise (PN), and the third term is the back action noise (BAN). As $\kappa^2 \propto N_{ph}N_a$, the BAN will grow quadratically as a function of the number of photons or atoms, while the spin projection noise will grow linearly.

The atomic state is considered to be a Gaussian state, hence the variance of the atomic state can be extracted from the experimental data with a measured

variance $\sigma^2_{measured}$. The atomic noise is calculated form the measured noise by

$$AN = \frac{\sigma^2_{measured} - SN - EN}{SN} \qquad (3.16)$$

and then normalized to the SN. The measurement of the noise of a system in the CSS, as a function of the atom number, is shown in figure 3.9, in which the quadratic growth of the atomic noise is due to the back-action noise. The atom number is changed by varying the power of the repump laser, which changes the population of the atoms in the F=3 ground state.
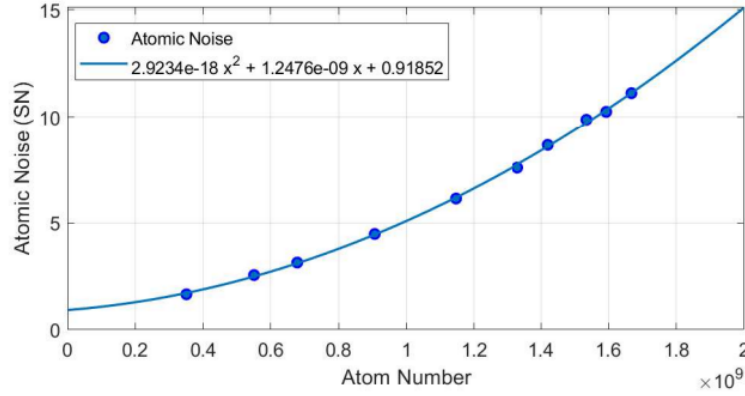

Figure 3.9.: The atomic noise of the CSS for various atom numbers. The blue cure is a quadratic fit

3.4.3 Spin projection Noise

The spin projection noise fundamentally limits the sensitivity of the atomic magnetometers. The spin projection noise is intrinsic to the atoms and it arises from the Heisenberg uncertainty of the spin components $\mathrm{Var}(\hat{J}_y) \cdot \mathrm{Var}(\hat{J}_z) \geq J_x^2/4$. To estimate the PN, the thermal noise method is used, where the atomic ensemble is measured without it being optically pumped. All of the magnetic sub-levels of the ground states are equally populated, leading to a fully symmetric system, called the thermal state, as can be seen in the following equation

$$\hat{J}_x^2 = \hat{J}_y^2 = \hat{J}_z^2 = \frac{F(F+1)}{3} = \frac{20}{3} \qquad (3.17)$$

when $\langle J_x \rangle = 0$. This means that in the measurement of this state there is no back action noise as the coupling of the light noise with the atomic spin, shown in equation 2.30, is negligible. With no BAN in the thermal state, the spin projection noise can be measured. The noise in the thermal state is calculated the same way as the atomic noise and is called the thermal noise.

The thermal noise at different probe power is shown in figure 3.10. The linear growth of the noise demonstrates that there is no BAN and classical noise in the measurement of this state.
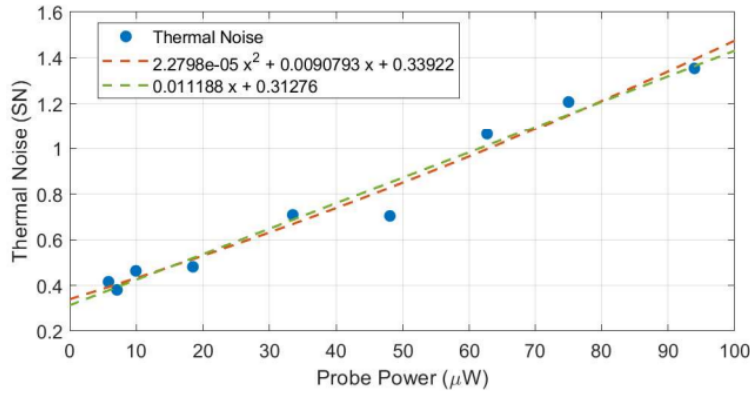

Figure 3.10.: The measured thermal noise in shot noise units of the thermal state as a function of the probe power. The dash red and green curves are the fit of a quadratic and linear functions

As the atomic ensemble is not in the CSS, the minimal noise state, the PN is larger in the thermal state. All of the magnetic sub-levels are equally populated, including those in the F=3 ground state, which are not observed. The observed PN will be $\frac{20}{3}\frac{9}{16}N_a = \frac{15}{4}N_a$ as there are 16 magnetic sub-levels, nine of which belong to the F=4 ground state. Compared to the PN in the CSS, which is $\frac{FN_a}{2} = 2N_a$, the PN in the thermal state is $\frac{15}{8}$ times larger than the PN in the CSS. However as the polarization is 97%, some atoms are in the $m_F = 3$ sub-level. The atomic ensemble is not in a perfect CSS, which leads to an increase of the atomic noise by approximately 15% [21].

Back-action evasion and spin squeezing

<div style="text-align: right;">4</div>

The precision of measuring two non commuting operators simultaneously, with the canonical atomic position $\hat{x}$ and momentum $\hat{p}$ and the commuting relation $[\hat{x}, \hat{p}] = i$, is limited by the Heisenberg uncertainty principle [30]. There are however no limits on how precise one operator is measured. If the system is in a so called squeezed state (SS), the uncertainty is lower than in the coherent state, for example $\text{Var}(\hat{x}) \leq 1/2$. To achieve a spin squeezing, the quantum state of the atoms needs to be sustained during the QND measurement. The decoherence time needs to be large as every decoherence event will cause loss of information of the operator. Stroboscopic QND or back-action evasion measurement is a method of generating a SS whereby only one quadrature is measured by applying a stroboscopic pulse at twice the Larmor frequency. The measured quadrature will not be altered from the BAN, while the other quadrature will be highly affected by the BAN.
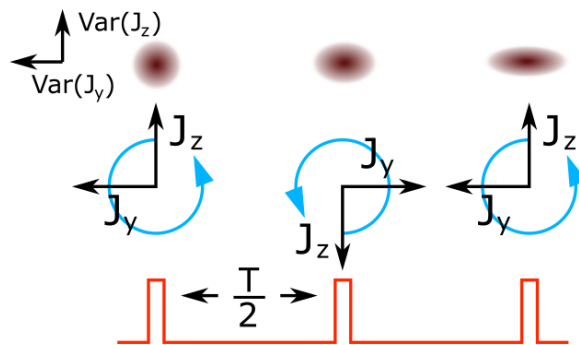

Figure 4.1.: Illustration of the stroboscopic probing and spin squeezing

4.1 Back-Action Evasion

To achieve a back-action evasion measurement with the setup, one of the conical variables is considered, expressed in the rotating frame as $\hat{X}(t) =$

$\hat{X}_0 \cos(\Omega t) + \hat{P}_0 \sin(\Omega t)$, with $\hat{X}_0 = \frac{\hat{J}_y}{\sqrt{J_x}}$ and $\hat{P}_0 = \frac{\hat{J}_z}{\sqrt{J_x}}$ [21]. The light atom interaction Hamiltonian can be approximated as $\hat{H}_{int} = 2\frac{\kappa}{\sqrt{N_{ph}J_x}}\hat{S}_z\hat{J}_z$ for a probe laser that is detuned far enough, $[\hat{H}_{int}, \hat{J}_z] = 0$. The probe laser consists of δ-pulses applied at times $t = 0, \frac{\pi}{\Omega}, \frac{2\pi}{\Omega}, ..., \frac{n\pi}{\Omega}$, as shown in figure 4.2. The noise of the probe laser will couple with $\hat{J}_y$ but not with $\hat{J}_z$ as the probe laser will be off during the measurement of $\hat{J}_y$. As the probe laser is only on when $\hat{J}_z$ is measured, $\hat{J}_y$ is not measured, and there is no BAN is $\hat{J}_z$, the back-action is evaded.
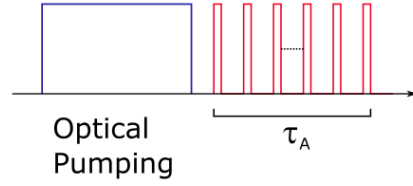

Figure 4.2.: Pulse sequence for back-action evasion measurement with a stroboscopic prob of duration τ_A

4.2 Theory

The Stokes operator $\hat{S}_y^{out}$ of the probe laser with stroboscopic intensity- modulation at twice the Larmor frequency is detected and its Fourier component $\cos(\Omega t)$, can be measured with the lock-in amplifier [30]. This causes the measurement of the atomic position operator $\hat{x}$ to be integrated over one Larmor spin rotation, weighed with a cosine wave from the demodulation done by the lock-in amplifier and with a pulse shape function from the stroboscopic pulse of the probe:

$$\hat{x}(kT) = \frac{1}{DT}\int_{kT}^{(k+1)T} \frac{\hat{J}_z}{\sqrt{J_x}}u(t)\cos(\Omega t)dt \qquad (4.1)$$

with $k \in \mathbb{N}$, T being the Larmor period $\frac{2\pi}{\Omega}$ and $u(t)$ a stroboscopic function with duty cycle D and defined as

$$u(t) = \begin{cases} 1 & \text{if} & -\frac{DT}{4} + kT \le t \le \frac{DT}{4} + kT \\ 0 & \text{if} & \frac{DT}{4} + kT < t < -\frac{DT}{4} + (k+\frac{1}{2})T \\ 1 & \text{if} & \frac{DT}{4} + (k+\frac{1}{2})T \le t \le \frac{DT}{4} + (k+\frac{1}{2})T \end{cases} \qquad (4.2)$$

The demodulation phase and frequency of the lock-in amplifier is optimized to match the stroboscopic phase, such that the overlap of the function $u(t)$ with the cosine quadrature of the lock-in amplifier is maximized. The measurement

of the shot noise of both the sine and cosine quadratures of the lock-in amplifier for different phases is shown in figure 4.3 and the signal of the cosine quadrature is maximal at the phase of .05 rad.
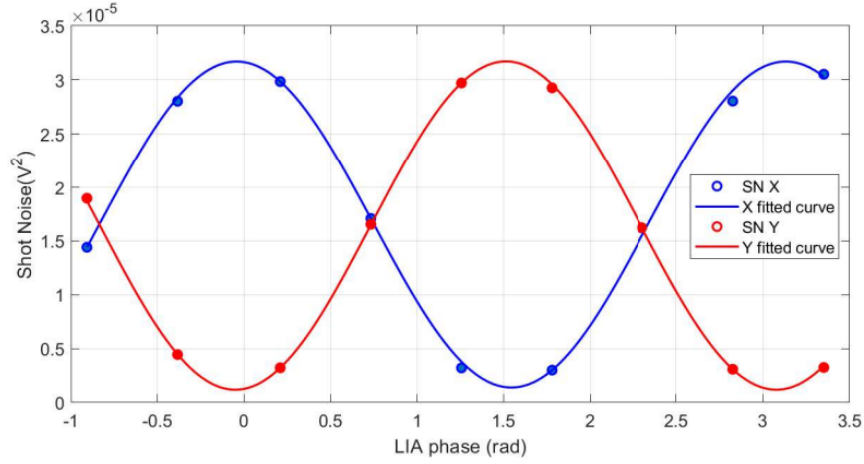

Figure 4.3.: The measured shot noise for various phases of the LIA, the cosine and sine quadrature are depicted in blue and red, respectively. The curve is a fitted cosine function

The measurement of the cosine quadrature of the Stokes operator $\hat{S}_y^{out} = \int_0^\tau \hat{S}_y^{out}(t) \cos(\Omega t) dt$ over a period duration of $\tau = NT$ can be written as

$$\hat{S}_{y,\tau}^{out} = \sum_{k=0}^{N} [\hat{Y}(kT) + a\bar{S}_x T \sqrt{J_x}\hat{x}(kT)] \tag{4.3}$$

$$\hat{Y}(kT) = \int_{kT}^{(k+1)T} \hat{S}_y^{in} u(t) \cos(\Omega t) dt \tag{4.4}$$

where $\bar{S}_x$ means the average over the Larmor period T and N is the number of complete Larmor rotations [21]. Equation 4.3 is of similar form as equation 2.34, the first term is responsible for the shot noise while the second term has information about the spin components. As there is no correlation between $\hat{S}_y^{in}$ and the spin components, $\langle \hat{S}_y^{in}(k_1 T)\hat{x}(k_2 T)\rangle = 0 \quad \forall k_1, k_2$.

The correlation for a coherent linearly polarized field in the y-direction is $\langle \hat{S}_y(t)\hat{S}_y(t')\rangle = \frac{S_x}{2}\delta(t - t')$ and $S_x = \frac{\Phi T}{2}$, where Φ is the photon flux, hence

$$\langle \hat{Y}(k_1 T)\hat{Y}(k_2 T)\rangle = \frac{\bar{\Phi}T}{8}[1 + sinc(\pi D)]\delta_{k_1 k_2} = \langle \hat{Y}^2\rangle\delta_{k_1 k_2} \tag{4.5}$$

where $\bar{\Phi}$ is the average photon flux over the Larmor period T and δ is the Kronecker delta.

The operator $\hat{x}$ can be written as the sum of two uncorrelated parts

$$\hat{x}(kT) = \hat{x}_{in}(kT) + \hat{x}_{BA}(kT) \tag{4.6}$$

and $\langle \hat{x}_{in}(k_1 T)\hat{x}_{BA}(k_2 T)\rangle = 0 \quad \forall k_1, k_2$ [30]. The first term in equation 4.6 is from the spin components of the initial quantum state of the system and gives rise to the spin projection noise.

$$\hat{x}_{in}(kT) = \frac{1}{TD}\int_{kT}^{(k+1)T} u(t)\cos{(\Omega t)}[\hat{X}_0 \cos{(\Omega t)} + \hat{P}_0 \sin{(\Omega t)}]dt = \frac{\hat{X}_0[1+\text{sinc}(\pi D)]}{2} \tag{4.7}$$

The spin projection noise is then

$$\langle \hat{x}_{in}^2 \rangle = \langle \hat{X}_0^2 \rangle \frac{[1+\text{sinc}(\pi D)]^2}{4} = \frac{[1+\text{sinc}(\pi D)]^2}{8} \tag{4.8}$$

The minimal uncertainty of the CSS is used, $\text{Var}(\hat{X}_0) = \frac{1}{2}$ as the conditional variance is compared to the CSS variance. The second term of the equation 4.6 describes the coupling of the quantum probe noise to the measured operator and leads to the BAN

$$\hat{x}_{BA}(kT) = \frac{1}{TD}\int_{kT}^{(k+1)T} u(t)\cos{(\Omega t)}\hat{X}_{BA}(t)dt \tag{4.9}$$

$$\hat{X}_{BA}(t) = a\bar{J}_x \int_0^t \sin{[\Omega(t-t')]}\hat{S}_z(t')dt' \tag{4.10}$$

It can be shown that, with the full derivation in ref [21],

$$\langle \hat{x}_{BA}(k_1 T)\hat{x}_{BA}(k_2 T)\rangle = \frac{[\mathcal{K}+2\text{min}(k_1,k_2)]a^2 J_x \bar{\Phi}T}{64}[1-\text{sinc}(\pi D)][1+\text{sinc}(\pi D)]^2 \tag{4.11}$$

where $\mathcal{K}$ is a numerical factor with values of

$$\mathcal{K}\begin{cases} = 1 & \text{if} \quad k_1 \neq k_2 \\ \approx 2.4 & \text{if} \quad k_1 = k_2 \end{cases} \tag{4.12}$$

In case of the measurement being over many cycles such that $\mathcal{K} \ll N$, the exact value of $\mathcal{K}$ is not relevant and the measured variance is

$$\text{Var}(\hat{S}_{y,\tau}^{out}) = N\langle\hat{Y}^2\rangle + \frac{a^2 J_x \bar{\Phi}^2 N^2 T^2}{4}\text{Var}(\hat{X}_0) + \frac{a^2 J_x \bar{\Phi}^2 T^2}{4}\sum_{k_1=0}^{N-1}\sum_{k_2=0}^{N-1}\langle \hat{x}_{BA}(k_1 T)\hat{x}_{BA}(k_2 T)\rangle \tag{4.13}$$

$$\text{Var}(\hat{S}_{y,\tau}^{out}) \approx \frac{\bar{\Phi}\tau}{8}[1+\text{sinc}(\pi D)]\left[1 + \tilde{\kappa}^2 + \frac{\tilde{\kappa}^4}{3}\frac{1-\text{sinc}(\pi D)}{1+\text{sinc}(\pi D)}\right] \tag{4.14}$$

where $\tau = NT$ is the total measurement time and the coupling constant is

$$\tilde{\kappa}^2 = \frac{1}{4}a^2 J_x \bar{\Phi}\tau[1 + \text{sinc}(\pi D)] \qquad (4.15)$$

The stroboscopic back-action coupling constant in equation 4.14 is

$$C = \frac{1 - \text{sinc}(\pi D)}{1 + \text{sinc}(\pi D)} \qquad (4.16)$$

and is shown in figure 4.4 for different duty cycles. When there is the ideal case of δ pulses, C=0 and there is no back-action a perfect QND measurement is possible. On the other hand if the probe is continuous, the duty cycle is 100% and the coupling constant is C=1.
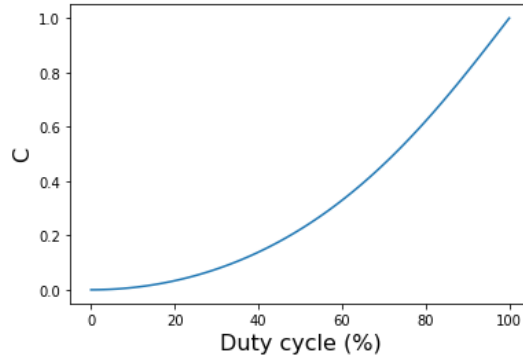

Figure 4.4.: The stroboscopic back-action coupling constant C as a function of the duty cycle D

4.3 Results

To generate the stroboscopic pulses, the acousto-optic modulator is used to stroboscopically modulate the intensity of the probe beam at twice the Larmor frequency with square pulses from a function generator. The width of the stroboscopic pulse is controlled by the duty cycle of the square pulse. The power of the probe averaged over one period is kept the same for the different duty cycle measurements. The measurements are repeated 1600 times to acquire the statistics to calculate the noise.

4.3.1 Light shot noise

The light shot noise for stroboscopic measurements is measured in a similar way as was described in section 3.4.1. The probe laser is stroboscopic intensity modulated at twice the Larmor frequency, then the constant magnetic field is changed so that the new Larmor frequency is a few line-width away from the bandwidth of the LIA. The noise from the atomic ensemble will be filtered out and only the light noise is measured as it has a white spectrum. The light shot noise is verified to scale linearly with the number of photons as shown in figure 4.5. The figure also shows that for the same photon number, the SN is higher for lower duty cycles D due to the different demodulation efficiency. The higher demodulation efficiency at lower duty cycles is due to more photons arriving closer to the maximum of the cosine quadrature and therefore are weighted more. The demodulation efficiency is shown in the $[1 + \mathrm{sinc}(\pi D)]$ term of equation 4.14.
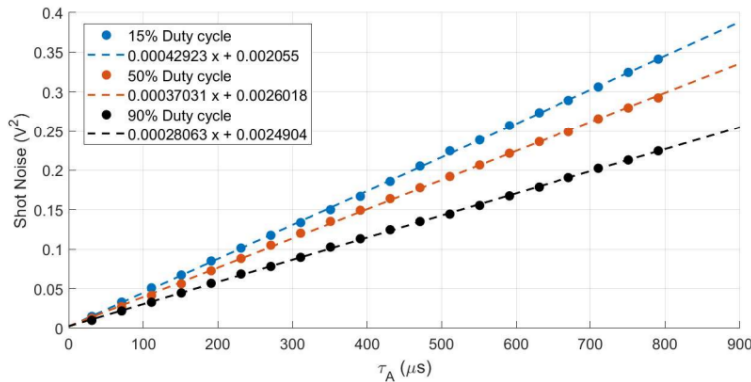

Figure 4.5.: The SN for various durations of the stroboscopic pulses τ_A. The 90%, 50%, and 15% duty cycles are depicted in black, red, and blue, respectively.

4.3.2 Atomic noise

The atomic noise for stroboscopic measurements of the CSS is calculated using equation 3.16 and is scaled to the spin projection noise. To calculate the PN of the CSS, the thermal noise is measured, as there is no BAN in the thermal state, only PN. The thermal noise is then multiplied by a factor of $\frac{8}{15}$, which gives the PN of the CSS as explained in section 3.4.3. The atomic noise at different pulse durations τ_A for various duty cycles is shown in figure 4.6. The

atomic noise scales linearly to the spin projection noise as the BAN grows quadratically as a function of photon number, while the PN grows linearly. The less BAN there is in a measurement, the slower the growth of the atomic noise; in the ideal case where there is no BAN, the atomic noise would only consist of the PN and the slope would be flat. The growth of the atomic noise at 15% duty cycle is significantly lower than for the atomic noise at 90% duty cycle (the normal probing comparison), showing that the BAN was mostly evaded. However there is still some BAN which will cause decoherence at higher photon numbers. More BAN can be evaded at a lower duty cycle, however the rise and fall times of the function generators for the stroboscopic pulses and the AOM reaction time limits how low the duty cycle can go.
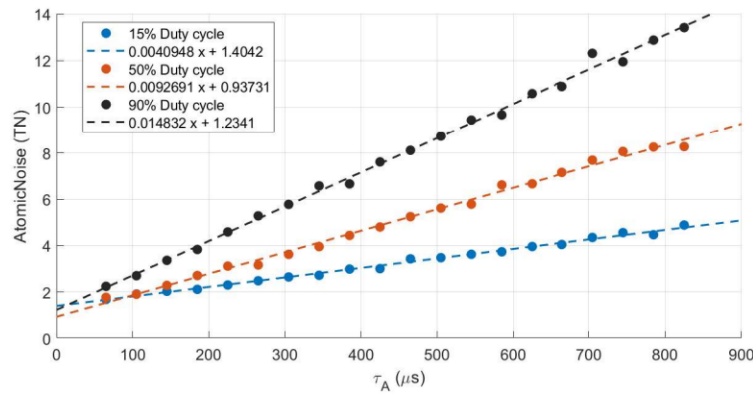

Figure 4.6.: The atomic noise for varying pulse duration, τ_A, in thermal noise units. The 90%, 50%, and 15% duty cycles are depicted in black, red, and blue, respectively

4.4 Spin Squeezing

For stroboscopic measurement that have sufficient back-action evasion, spin squeezing can be achieved such that the sensitivity is lower than the SQL [21]. For a back-action evasion measurement the input/output equations can be written as

$$\begin{aligned}
\hat{y}^{out} &= \hat{y}^{in} + \tilde{\kappa}\hat{p}^{in} \\
\hat{p}^{out} &= \hat{p}^{in}
\end{aligned}$$

$$(4.17)$$

where $\hat{y}$ and $\hat{p}$ are the conical operators of light position and atoms momentum respectively. They both have Gaussian distributions as there are a large number

of photons and atoms, The formula for the conditional variance of a Gaussian distribution is

$$\text{Var}(A|B) = \text{Var}(A) - \frac{\text{Cov}^2(A, B)}{\text{Var}(B)} \tag{4.18}$$

where $\text{Cov}(A, B)$ is the covariance between A and B. For a system prepared in the CSS, the variance of the spin component conditioned on the light operator $\hat{y}$ is

$$\text{Var}(\hat{p}|\hat{y}) = \frac{1}{2}\frac{1}{1 + \tilde{\kappa}^2} \tag{4.19}$$

The squeezing generated after a back-action evading measurement of time $\tau = NT$ of the stroboscopic modulation of the probe, called stroboscopic squeezing, and assuming that there is no decoherence is defined as

$$\xi_0^2 = \frac{\text{Var}[\hat{x}(NT)|\hat{S}_{y,\tau}^{out}]}{\text{Var}(\hat{X}_0)} \tag{4.20}$$

with $\text{Var}(\hat{X}_0)$ as the spin projection noise while $\hat{S}_{y,\tau}^{out}$ is the measurement recorded of the cosine quadrature. The conditional variance of the collective spin components $\hat{x}(NT)$ is given by

$$\text{Var}[\hat{x}(NT)|\hat{S}_{y,\tau}^{out}] = \text{Var}[\hat{x}(NT)] - \frac{\text{Cov}^2[\hat{x}(NT), \hat{S}_{y,\tau}^{out}]}{\text{Var}(\hat{S}_{y,\tau}^{out})} \tag{4.21}$$

and the covariance between $\hat{x}(NT)$ and $\hat{S}_{y,\tau}^{out}$ is

$$\begin{aligned}
\text{Cov}^2\left[\hat{x}(NT), \hat{S}_{y,\tau}^{out}\right] &= \frac{a\sqrt{J_x}\bar{\Phi}T}{2}\left[N\text{Var}(\hat{X}_0) + \sum_{k=0}^{N-1}\langle\hat{x}_{BA}(NT)\hat{x}_{BA}(kT)\rangle\right] \\
&\approx \frac{a\sqrt{J_x}\bar{\Phi}\tau}{16}[1 + \text{sinc}(\pi D)]^2\left[1 + \frac{\tilde{\kappa}^2}{2}\frac{1 - \text{sinc}(\pi D)}{1 + \text{sinc}(\pi D)}\right]
\end{aligned} \tag{4.22}$$

where the unconditional variance of $\hat{x}(NT)$ is

$$\begin{aligned}
\text{Var}[\hat{x}(NT)] &= \text{Var}(\hat{X}_0) + \langle\hat{x}_{BA}(NT)\hat{x}_{BA}(NT)\rangle \\
&\approx \text{Var}(\hat{X}_0)\left[1 + \frac{\tilde{\kappa}^2}{2}\frac{1 - \text{sinc}(\pi D)}{1 + \text{sinc}(\pi D)}\right]
\end{aligned} \tag{4.23}$$

Combining the previous equation into equation 4.20, the squeezing is

$$\xi_0^2 \approx 1 + \tilde{\kappa}^2 \frac{1 - \text{sinc}(\pi D)}{1 + \text{sinc}(\pi D)} - \frac{\tilde{\kappa}^2 \left[1 + \frac{\tilde{\kappa}^2}{2} \frac{1 - \text{sinc}(\pi D)}{1 + \text{sinc}(\pi D)} \right]}{1 + \tilde{\kappa}^2 + \frac{\tilde{\kappa}^4}{3} \frac{1 - \text{sinc}(\pi D)}{1 + \text{sinc}(\pi D)}} \tag{4.24}$$

for the ideal case where $\delta-$pulse is used, the duty cycle is 0 and the squeezing becomes $\xi_0^2 = 1/(1 + \tilde{\kappa}^s)$ as shown in the equation 4.19.

The derivation of the squeezing was done with the assumption that there was no decoherence. The inclusion of decoherence will cause the squeezing to relax, reducing it to [30]

$$\xi^2 \approx \xi_0^2 + \eta_\tau \tag{4.25}$$

η_τ is a variable that depends on the decay mechanisms and scales with the number of decoherent events during the measurement time τ.

4.4.1 Conditional variance and Squeezing Results

To achieve spin squeezing, two sets of stroboscopic pulses are used as shown in figure 4.7. The first, τ_A, provides information about the observable $\hat{x} = \hat{J}_z/\sqrt{J_x}$ and the second, τ_B, evaluates the variants of the observable, conditioned on the first measurement.
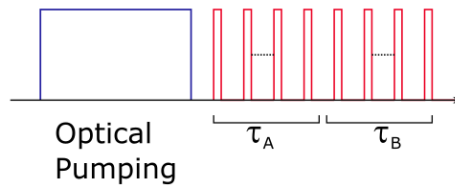

Figure 4.7.: Pulse sequence for conditional spin squeezing with the first and second stroboscopic prob pulses of duration τ_A and τ_B, respectively

The results of the first and second pulses are denoted as Q_A and Q_B, respectively. The correlation between the two pulses can be described by the parameter $\alpha_{opt} = \text{Cov}^2(Q_B, Q_A)/\text{Var}(Q_A)$ [31]. This parameter minimizes the conditional variance of the conditional results, $Q_C = Q_B - \alpha Q_A$.

$$\text{Var}(Q_B|Q_A) = \min(\text{Var}(Q_C)) = \text{Var}(Q_B - \alpha_{opt}Q_A) \tag{4.26}$$

If $\alpha_{opt} = 1$, there would be perfect correlation between the two pulses and if $\alpha_{opt} = 0$, there would be no correlation between the pulses. Their variance is calculated by

$$\text{Var}(\hat{x}_{A/B}) = \frac{\text{Var}(Q_{A/B}) - SN_{A/B} - EN_{A/B}}{SN_{A/B}} \tag{4.27}$$

where $SN_{A/B}$ and $EN_{A/B}$ are the shot noise and the electric noise of a pulse with the duration of $\tau_{A/B}$. The conditional variance is then

$$\begin{aligned}
\text{Var}(\hat{x}_B | \hat{x}_A) &= \frac{\text{Var}(Q_B | Q_A)}{SN_B} - 1 - \frac{EN_B}{SN_B} \\
&= \frac{\text{Var}(Q_B)}{SN_B} - \frac{\text{Cov}^2(Q_B, Q_A)}{SN_B \text{Var}(Q_A)} - 1 - \frac{EN_B}{SN_B}
\end{aligned} \tag{4.28}$$

The conditional and unconditional atomic noise of the second pulse for different τ_A and τ_B duration is shown in figure 4.8. The expected spin projection noise for the CSS is also plotted for comparison. The PN of the CSS is calculated by multiplying the PN of the thermal state by a factor of $\frac{8}{15}$ as explained in section 3.4.3. From the correlation between the first and second pulse, the conditional atomic noise is significantly lower than the unconditional atomic noise and lower than the spin projection noise. The result also shows that spin squeezing is achieved, as the conditional atomic noise is lower than the spin projection noise of the CSS, which is the minimal uncertainty state.

To select the optimal duration of the two pulses, τ_A and τ_B, a histogram is made of squeezing achieved for different τ_A and τ_B duration, which is shown in figure 4.9a. The degree of squeezing is calculated by $10 \log(\xi^2)$ [21], where

$$\xi^2 = \frac{\text{Var}(\hat{x}_B | \hat{x}_A)}{\text{Var}(\hat{x}_B)} \tag{4.29}$$

The optimal duration of the two pulses τ_A and τ_B, depend on coupling strength and the decoherence. A stronger coupling strength would mean that more information is gained from the atoms and a longer decoherence time will cause less information to be destroyed. From the histogram (figure 4.9a), the best squeezing achieved is -4.5 ± 0.7 dB at a τ_A and τ_B duration of 220 and 40 μs, respectively. τ_A was therefore chosen to be 220 μs. As for τ_B, while better squeezing is achieved at lower duration, as shown in figure 4.9c, the noise is however dominated by the SN. This is clearly demonstrated in figure 4.8b, at a
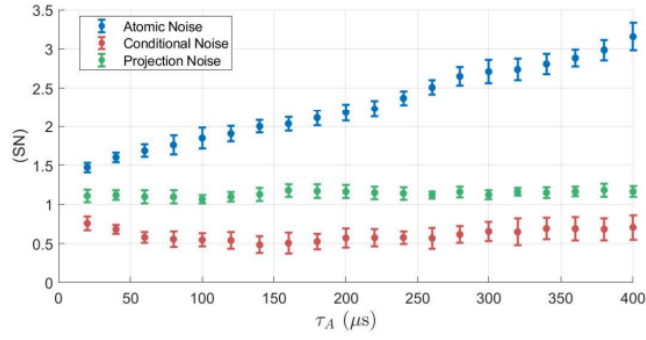
(a) For various duration of τ_A for $\tau_B = 40$ μs
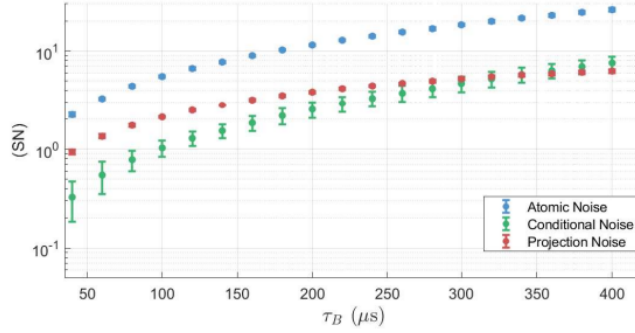
(b) For various duration of τ_B for $\tau_A = 220$ μs

Figure 4.8.: The atomic noise, conditional noise and projection noise are in blue, red and green respectively in SN units for 15% duty cycle [18]

τ_B of 40 μs the AN and CN are 2.2 ± 0.1 and 0.3 ± 0.1 times the SN, respectively, leading to a total noise reduction of $60 \pm 0.5\%$. However at a τ_B of 100 μs, the AN and CN are 25.5 ± 0.2 and 1.0 ± 0.2 times the SN, respectively, leading to a larger total noise reduction of $70 \pm 0.7\%$. Therefor τ_B is selected to be 100μs where the noise is no longer dominated by the SN.

Increasing the probe power to increase the coupling strength would lead to more squeezing, but it would also increase the BAN and SN. Reducing τ_B would also increase the the squeezing, however if τ_B is close to the the averaging time of the LIA, less noise would be suppressed from the LIA.

4.4.2 Squeezing with a RF Pulse

The pulse sequence for MIT measurements is shown in figure 4.10. The RF pulse is needed in between τ_A and τ_B to generate a secondary magnetic field from the sample, which is explained in section 5.1. Any disruption to the atomic ensemble will cause decoherence and a reduction in squeezing which is shown in figure 4.11. Figure 4.11a shows the reduction of squeezing caused
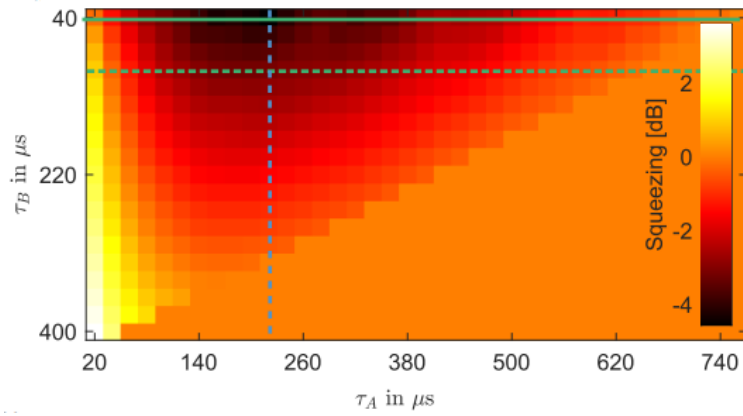
(a) A histogram of the squeezing achieved for various τ_A and τ_B durations at 15% duty cycle. The solid green line and the dash blue line depict the slices shown in (b) and (c), respectively.
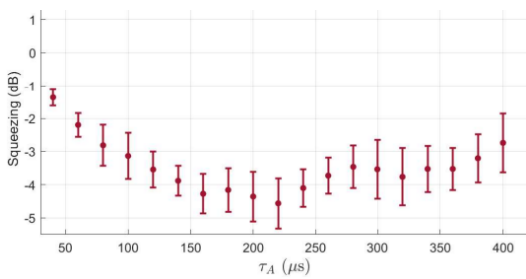
(b) The squeezing achieved for various duration of τ_A for $\tau_B = 40\ \mu s$
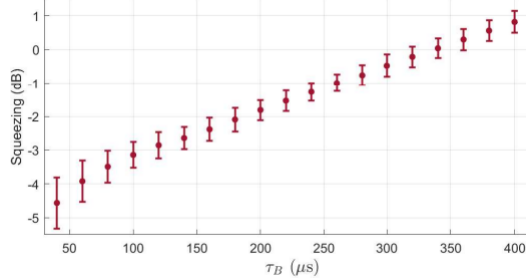
(c) The squeezing achieved versus the duration of τ_B at $\tau_A = 220\ \mu s$

Figure 4.9.: [18]

by the gap due to decay time of the spins. The gap is set to 50 μs as to allow the encoding of the magnetic information into the atomic state. The squeezing does not seem to be dependent on the amplitude of the voltage applied of the RF pulse as shown in figure 4.11b. The RF pulse simply displaces the spin, giving it a transverse component and it is off when the atomic ensemble is probed and thus the voltage applied would not affect the squeezing. While the RF is off, having the wire connected will add some noise from the RF coils, decreasing the squeezing.
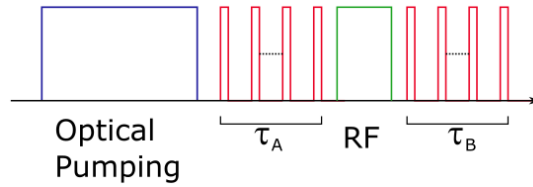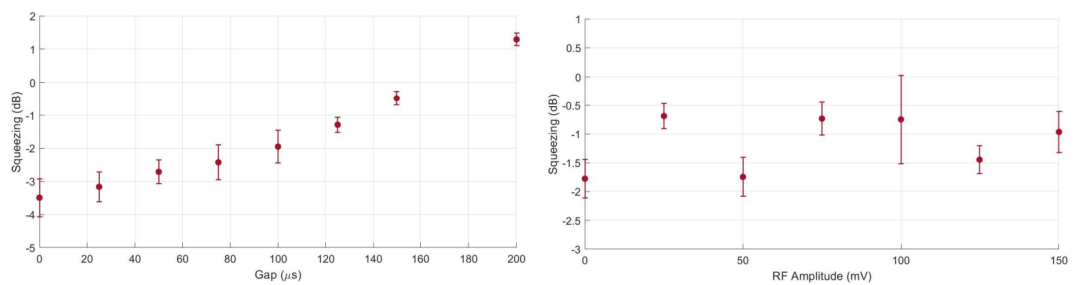
Figure 4.10.: Pulse sequence for a MIT measurement with a RF pulse, and the first and second stroboscopic prob pulses of duration τ_A and τ_B, respectively

(a) The squeezing achieved for different gaps of the RF pulse without any applied voltage

(b) The squeezing achieved for various applied voltage of RF pulses, with the duration of the gap set to 50 μs

Figure 4.11.

MIT

A two coil differential system was used for the MIT measurements. The first coil was used to induce eddy currents, that generate a secondary magnetic field in the sample. The second coil is there to generate a magnetic field that cancels out the magnetic field of the first coil at the cell position. With this setup measurements can be done at a stronger secondary magnetic field, as the effect of power broadening from the primary magnetic field, which reduced the signal size, are removed [27].

The sample used for the MIT measurements is a $10\,\mathrm{mm}$ by $10\,\mathrm{mm}$ by $1\,\mathrm{mm}$ piece of titanium and has a conductivity of $2.4 \times 10^6\,\mathrm{S\,m^{-1}}$. Titanium is weakly magnetic, and observing an object that has low magnetic susceptibility by measuring its response to external magnetic field is usually difficult. Therefore measurements with titanium are a good benchmark

5.1 Eddy current theory and simulations

Eddy currents are closed loops of current in conductive objects. The currents are induced from a changing magnetic field and flow within the conductor in a plane perpendicular to the primary magnetic field to generate a magnetic field to oppose the change of the primary magnetic field. The primary magnetic field is attenuated exponentially when penetrating the object due to the skin effect. The skin depth is $\delta(\omega) \approx \sqrt{2/(\omega\mu_0\sigma)}$. The formula describes the penetration capability of the primary field into the conductive object, where ω is the angular frequency of the primary field, σ is the conductivity of the conductor and μ_0 is the vacuum permeability, assuming that the object is nonmagnetic [16].

The magnetic field generated from the eddy currents induced by the top coil from the setup shown in figure 5.1, are simulated using the python package Bfieldtools. This python package models magnetic fields using surface current
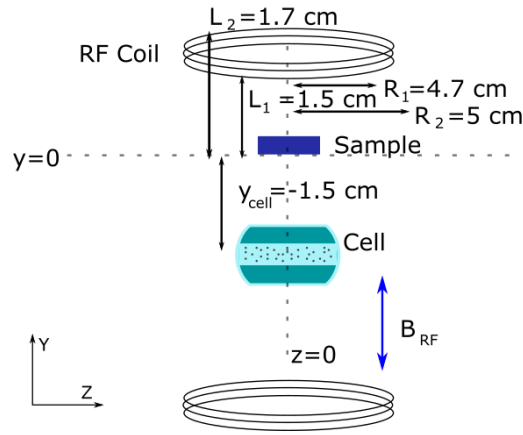
densities, which are represented by stream functions on triangle meshes [32] [33]. With this package, the mutual inductance of the coil to the sample can be calculated and is then used to compute the secondary field created from the eddy currents. However, it calculates the eddy currents from a primary field that has the form of a step function and simulates the decay of the eddy currents. For a primary magnetic field that is an oscillating sine wave, the secondary field is assumed to have the shape of the simulation without any decay.

The magnitude and phase of the secondary magnetic field at the center of the cell were calculated using Maxwell's equations by solving the differential equations of the vector potential to get a "closed-from" solution. The sample is assumed to be a linear, isotropic, homogeneous medium and to be operated in the quasi static regime, where the currents generated by changing electric fields in the sample can be ignored. Using the calculated results derived in [24] and [34], the secondary magnetic field from the eddy currents in the y-direction is given by

$$B_{eddy} = \int_0^\infty \frac{1}{2\alpha} I_0 \mu_0 I(\alpha, R_1, R_2) e^{\alpha y} K(\alpha, \alpha_1, T)(e^{\alpha L_2} - e^{\alpha L_1}) d\alpha \qquad (5.1)$$

where I_0 is the current in the coil, R_1 and R_2 are the coil inner and outer radii, T is the thickness of the sample, y, L_1 and L_2 are the distances of the cell, top and bottom of the coil from the sample, respectively. α is a separation

variable that is introduced when solving the vector potential using separation of variables and $\alpha_1 = \sqrt{\alpha^2 + i\omega\mu_0\sigma}$. $I(\alpha, R_1, R_2)$ is defined as

$$
\begin{aligned}
I(\alpha, R_1, R_2) = \frac{\pi}{2} & (R_2[J_1(R_2\alpha)H_0(R_2\alpha) - J_0(R_2\alpha)H_1(R_2\alpha)] \\
& - R_1[J_1(R_1\alpha)H_0(R_1\alpha) - J_0(R_1\alpha)H_1(R_1\alpha)])
\end{aligned}
\tag{5.2}
$$

where H_0 and H_1 are zeroth and first order Struve functions of the first kind and J_0 and J_1 are zeroth and first order Bessel functions of the first kind. $K(\alpha, \alpha_1, T)$ is defined as

$$
K(\alpha, \alpha_1, T) = \frac{(\alpha + \alpha_1)(\alpha_1 - \alpha_1) + (\alpha - \alpha_1)(\alpha_1 + \alpha)e^{2\alpha_1 T}}{(\alpha - \alpha_1)(\alpha_1 - \alpha_1) + (\alpha + \alpha_1)(\alpha_1 + \alpha)e^{2\alpha_1 T}}
\tag{5.3}
$$

The eddy current was then numerically calculated and the ratio of the amplitude of the secondary magnetic field to the amplitude of the primary magnetic field, $|B_{\text{eddy}}|/|B_1|$ as a function of frequency is shown in figure 5.2a. The magnetic field strength of the top coil was calculated using the formula for the on axis magnetic field of a coil

$$
B_1 = \frac{\mu_0 I_0 R^2}{2(R^2 + y^2)^{3/2}}
\tag{5.4}
$$

The simulation shows that for low frequencies the amplitude of the secondary magnetic field grows linearly until it becomes saturated. This is due to the skin effect, figure 5.2a. The skin depth decreases with increasing frequency, which forces the current to flow in a smaller cross section of the conductor, increasing the current density and the effective resistance. As for the phase, figure 5.2b shows the secondary field is $-90°$ and $-180°$ out of phase from the primary field at low and high frequencies, respectively. The shape of the secondary magnetic field along the path of the probe at a frequency of 720kHz is shown in figure 5.2c. The component B_z of the magnetic field has a mean of zero due to symmetry, so it does not affect the signal strength, but it makes the magnetic field inhomogeneous which would increase the decay rate, depending on the thermal averaging of the atomic ensemble.
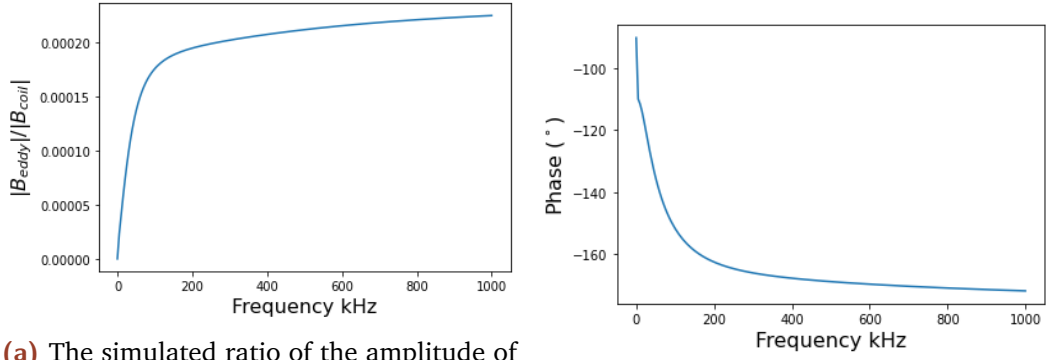
(a) The simulated ratio of the amplitude of the magnetic field caused by the eddy currents in the sample to the amplitude of the magnetic field form the RF coil for different operating frequencies

(b) The phase of the magnetic field caused by the eddy currents in the sample in relation to the magnetic field from the RF coil for different operating frequencies
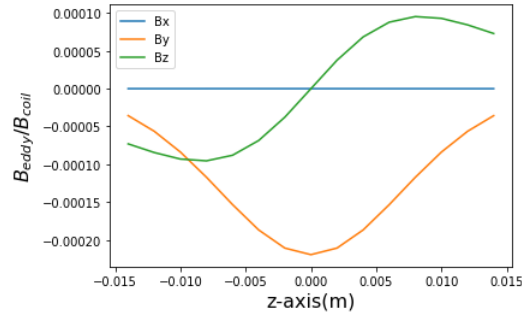
(c) The components of the magnetic field caused by the eddy currents in the sample along the path of propagation, with the cell at the center

Figure 5.2.: The results of the simulations

5.2 Sample Measurement

The coils are in an anti-Helmholtz configuration, such that the magnetic field produced by the coils at the cell are canceled out by one another. The secondary field causes the spin to have a transverse component, shifting the measurements of Q_B. The sample is placed above the cell and the measurements are done with and without the sample. The unconditional and conditional signal form the eddy current are calculated by

$$
\begin{aligned}
S_0 &= Q_B' - Q_B \\
S_C &= Q_C' - Q_C
\end{aligned}
\tag{5.5}
$$

where the $'$ and $_C$ denote the measurements done with the sample and the conditional measurements, respectively. The conditional measurement is given by $Q_C = Q_B - \alpha_{opt}Q_A$, where α_{opt} is the optimal feedback parameter.

5.2.1 RF phase

During the measurements, the atomic ensemble is not measured most of the time as the probing is stroboscopic. Therefore what is measured depends considerably on how all of the phases are aligned. It has been previously shown (section 4.2) how the phase between the demodulation signal of the LIA and the stroboscopic pulse affects the demodulation efficiency. The phase between the RF pulse and the stroboscopic pulse will affect the signal measured, most notably the signal from the eddy currents. The phase could also suppress the background signals and evade the noise from the residual RF fields.

From the simulations, the secondary magnetic field, caused by the eddy current, is expected to be -170° out of phase from the RF coils magnetic field. The phase of the secondary magnetic field is verified experimentally by measuring the signal with and without the sample as a function of the RF phase and is shown in figure 5.3a. For the measurement without the sample the current of the two coils are in the same direction making a pair of Helmholtz coils. This is necessary, as the anti-Helmholtz configuration used for measurements with the sample will cancel the signal from the coils. The results show that the secondary field is $-196°$ out of phase. The difference between the simulated and experimental phase shift could be caused by background signals, such as the eddy currents in the aluminum shield layer. Also the coils in the Helmholtz and anti-Helmholtz configurations have different impedances, which cause some additional phase shift.

The phase between the RF field and the demodulation signal of the LIA can cause suppression of background signals due to imperfect cancellations and could evade some of the noise from RF fields or from the sample. To see how this affects the correlation between the two pulses and the squeezing, the optimal feedback parameter α_{opt} and the squeezing are measured with and without the sample as a function of the phase of the RF field, shown in figure 5.3b and 5.3c. It shows that the average squeezing is about -1.8 ± 0.2 dB and that the α_{opt} and the squeezing do not depend on the phase of the RF field. The sample does not affect α_{opt} and the squeezing. Therefore the magnetic field inhomogeneity produced by the sample are not significant. The signal from the eddy currents as a function of the RF phase with the unconditional, conditional and spin projection noise is shown in figure 5.4. The insert in
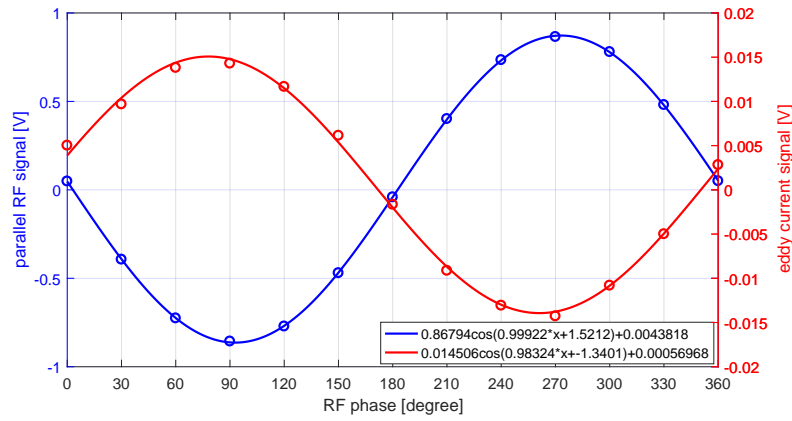
(a) The signal strength
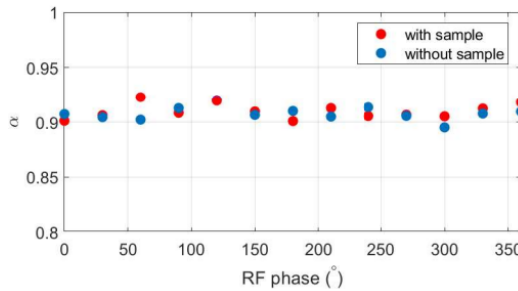
(b) The optimal feedback parameter α_{opt}
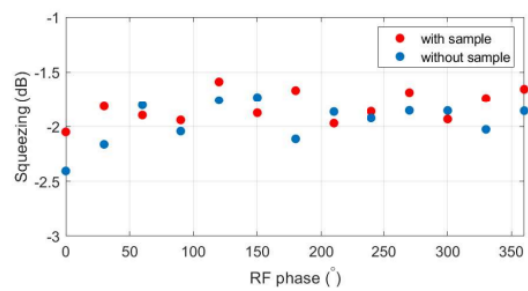
(c) The squeezing

Figure 5.3.: The results of various parameters as a function of the RF phases. The measurements done with the sample are depicted in red, while the ones without the sample are in blue [18]

the figure shows the distribution of the 16000 repetitions. The conditional uncertainty is about 39.7% less than the unconditional uncertainty and 10.5% below the SQL.

5.2.2 Moving the sample

The sample is moved over the cell by steps of 1 mm, and the signal from the eddy current is measured to make a one dimensional scan of the sample. The measurement is repeated 4000 times for each position and the results are shown in figure 5.5. The results are fitted with a Gaussian curve with the peak at the center of the sample. The signal to noise ratio is defined as the maximum change in signal over the uncertainty [27]. With the unconditional uncertainty, the SNR is $.725$, whereas with the conditional uncertainty, the SNR is 1.26, which is about a 73% increase.
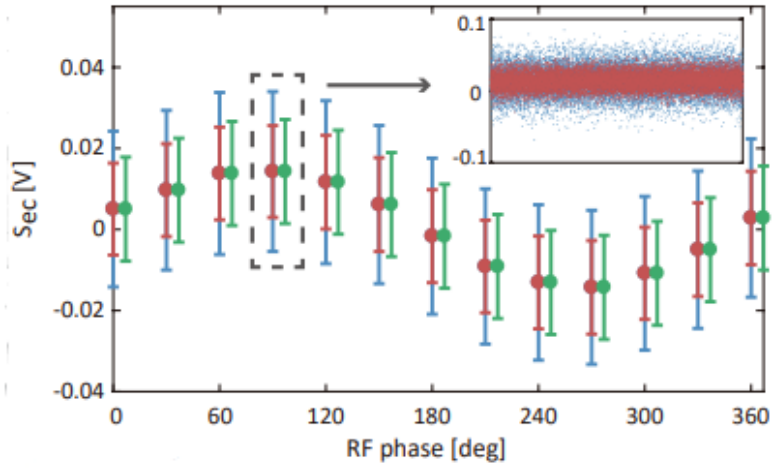
Figure 5.4.: The eddy current signal for different RF phases, the blue and red error bars represent the unconditional and conditional uncertainty, respectively. The green error bars are shifted to the side and represent the SQL [18]
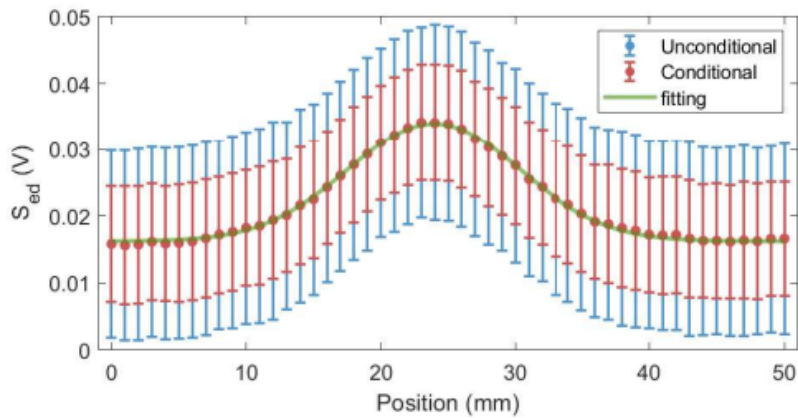

Figure 5.5.: The eddy current signal at different positions of the sample, the blue and red error bars are the unconditional and conditional uncertainty, respectively. The green curve is the fit of a Gaussian curve [18]

Conclusion

In summary, back-action evasion measurements were demonstrated by stroboscopically modulating the probe at twice the Larmor frequency. The BAN at 15% duty cycle is significantly reduced when comparing to the non stroboscopic probing (90% duty cycle). The increase in decoherence time from of the back-action evasion measurements allow for conditional spin squeezing, which was used to reduce the noise below the SQL. For the optimal duration of 220 and 40 μs of the two stroboscopic pulse, τ_A and τ_B, more than -4.6 ± 0.8 dB of squeezing was achieved. However in those measurements, the noise was dominated by the SN, which is not affected by the squeezing, leading to a low reduction of the total noise. The duration of τ_B was set to 100 μs, where the atomic noise was five times the SN and the squeezing was 3.1 ± 0.4dB. When the squeezing was lower, the total reduction of noise was higher as it was dominated by the atomic noise. The inclusion of the gap and the RF pulse is required to do MIT, even though it reduces the squeezing to 1.8 ± 0.2dB.

As for the MIT results, in the simulation the calculated phase of the secondary field generated by the eddy current was smaller than what was seen in the experiment, which could have been caused by background signals generated by the RF coils. A promising result was, that the squeezing was not affected by the RF phase. Therefor suppressing or intensifying certain signals can be done without affecting the squeezing, as signals depend on the RF phase. The conditional uncertainty is about 10% less than the spin projection noise, overcoming the SQL. A one dimensional scan of the sample was done and the SNR was improved by 70% through spin squeezing.

Outlook

The work done in this project on MIT imaging is far from finished. There are several things that can be done to improve the measurements. One important step would be working at a higher Lamor frequency, which should decrease the noise. However the available electronic equipment does not allow further research, as the stroboscopic pulses are too short. Another step would be to improve the coupling constant, κ, by coupling the micro cell with an optical cavity. The optical depth of the cell could be enhanced and increase the amount of information gained [21]. The effect of the eddy current in the aluminum shield also needs to be investigated. The eddy current flows on the surface of the shield and by scratching the inside of the shield, the flow of the eddy current is disrupted, which weakens the field generated by the current [35]. For further improvement the resolution of the setup needs to be measured, which could be done by cutting a hole in the sample. A smaller coil size should be tested to see if the resolution is ameliorated as it would make a more localized eddy current.

The MIT of the titanium sample acts as proof of concept to show that the SQL is surpassed and that there is an increase in the SNR. To implement successfully MIT for biomedical applications, such as MIT of the heart, there are a few issues that need to be overcome. One is that the eddy currents induced in the heart are very weak, therefore the sensitivity of the magnetometer need to be improved further by optimizing the squeezing. Besides that, background signals that interfere with the signals of the heart need to be suppressed. The MIT measurements and the heart beats need to be synchronized, as the heart beat produces its own magnetic field that mixes with the signal from the MIT.

Appendix

A.1 Main magnetic field homogeneity

To generate a constant homogeneous magnetic B_{bias} along the x-axis, a coil system was utilized. The coil system is composed of many coils that are placed between the μ metal and the aluminum layer of the shield (figure A.1). The main magnetic field was generated by six coils with different numbers of windings that are separated equidistantly along the shield[36]. Then to correct for any inhomogeneity along the direction of propagation (z-axis), two sets of coils were used. One is simply a pair of coils in the Helmholtz configuration in the middle of the shield, called the compensation coils. The other is made up of four rectangular coils, which are wrapped around the shield called the saddle coils.

To characterize the magnetic field produced by each coil system, a small cubic vapor cell was used to measure the Larmor frequency at different positions along the direction of prorogation [28]. The Larmor frequency was measured by measuring the MORS signal of the thermal state twice, once with the current flowing one way and the other with the current flipped. When the x component of the background static magnetic field was aligned with the magnetic field of the coils, the Larmor frequency was increased, and when the

Figure A.1.: picture of the coil system around aluminum layer of shield

current was flipped, the Larmor frequency was lower. To remove this the mean of the two measurements was used to estimate the Larmor frequency.

The strength of the magnetic field can be calculated from the Larmor frequency using $\Omega = g_F \mu_B B/\hbar$ where μ_B is the Bohr magneton and g_F is the Landé factor. The magnetic field of each coil set along the path of propagation is shown in figure A.2. The magnetic field of the three coil sets are then scaled and combined as to make B_{bias} a homogeneous field, which is plotted in figure A.2d.
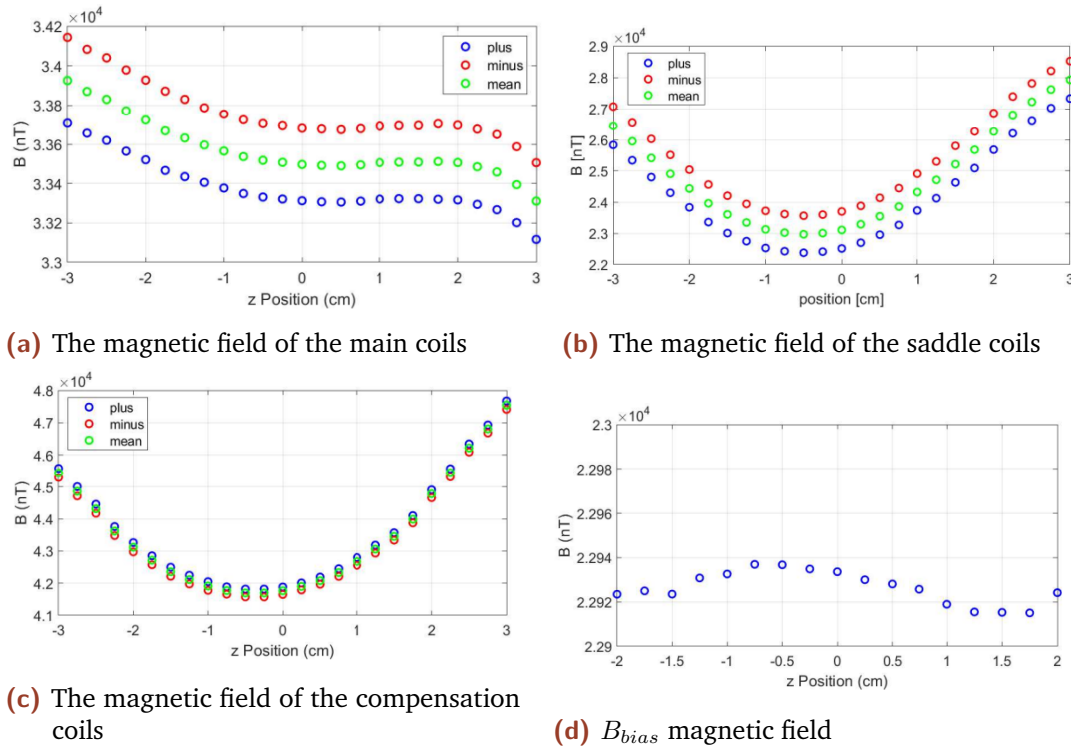

(a) The magnetic field of the main coils

(b) The magnetic field of the saddle coils

(c) The magnetic field of the compensation coils

(d) B_{bias} magnetic field

Figure A.2.: Measurements of the magnetic field along the path of propagation of the probe

A.2   RF Magnetic field calibration

A function generator is used to apply a sinusoidal current at the Larmor frequency to the RF coils, to generate the RF magnetic field. To calibrate the magnetic field a pick up coil with a radius $r = 4.5$ mm, $N_w = 30$ windings and the inductance L is used. To experimentally calculate the inductance L, the coil was connected to a series circuit with a resistor having resistance R and a function generator that applies an oscillating voltage. For an applied voltage with a frequency ω, the voltage, U over the resistor R is [23]

$$|U| = R|\epsilon| \left\{ \frac{\omega^2 L^2}{[1 - (\omega/\omega_{res})^2]^2} + R^2 \right\} \tag{A.1}$$

where ω_{res} is the resonance frequency of the coil. The voltage, U, was measured for various frequencies with an applied voltage of .5 V and a resistance of 50.6 Ω, as shown in figure A.3. From the parameters of the fit function, the inductance is 30.5μH. The oscillating magnetic field from the RF coil
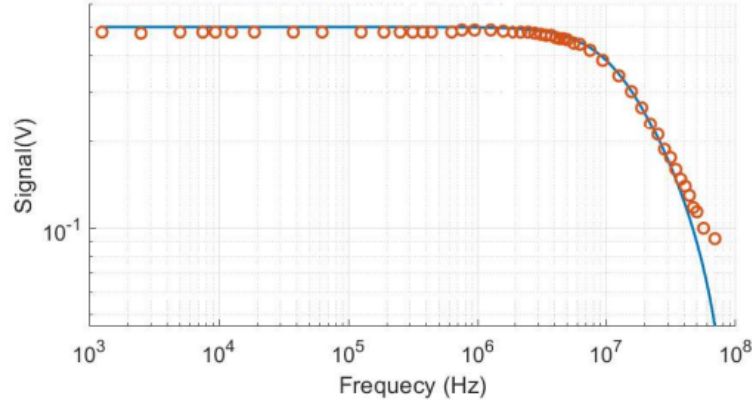

Figure A.3.: The voltage over the resistor for various frequencies from the function generator. The solid blue line is a fit.

creates a flux through the pick up coil, which then generates an electromotive force. The pick up coil is connected to a oscilloscope that measures the power $P_o = U_o^2/R_m$, over the resistance $R_m = 50\Omega$. The amplitude of the voltage is $U_\omega = \sqrt{2}U_o$ as U_o is a rms voltage. The magnetic field is then calculated by

$$|B_{RF}| = \frac{|1 + Z/R_m||U_\omega|}{N_w A \omega} \tag{A.2}$$

where A and Z are the area and the impedance of the coil, respectively. For high frequencies, that are below the resonance frequency of the coil, the impedance of the coil can be approximated as $Z \approx \omega L$. At the operating frequency $f = 720\text{kHz} = 2\pi\omega$, the impedance is $Z = i\,34\Omega$ and the magnetic field of the RF coil is a function of applied voltage as shown in figure A.4
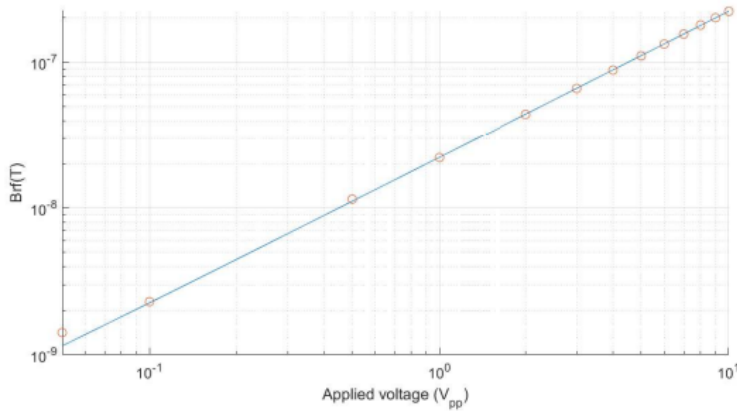
Figure A.4.: The measured magnetic field of the RF coil for different applied voltages

A.3 Varying the Atom Number

The atomic density is calculated by measuring the absorption spectrum of the cell [37]. The probe laser is scanned over the two hyperfine ground states and when it is on resonance with an atom, the probe light will scatter. The scattered light reduces the transmission causing dips in the absorption spectrum. The absorption cross section is then used to calculate the atomic density.

There are a few ways to change the number of atoms that the probe interacts with. The most basic method is to heat the cell, which increases the atomic density there in. The draw back of this method is, that the temperature takes a few hours to stabilize, which makes it hard to compare any measurement taken at different temperatures due to the drifts in current in the setup. That is why the atom number was instead varied by the repump laser, as stated in section 2.4. The repump excites the atoms in the $F = 3$ ground state, which then decays into either the $F = 3$ or 4 ground states. This changes the population of atoms in the $F = 4$ ground state, which is the population that interacts with the probe. The population of the atoms in this state is proportional to the square root of the area under the power spectrum density (PSD) [20]. For sufficiently strong enough repump power, it is assumed that the $F = 3$ ground state is emptied and that all atoms are in the $F = 4$ ground state.
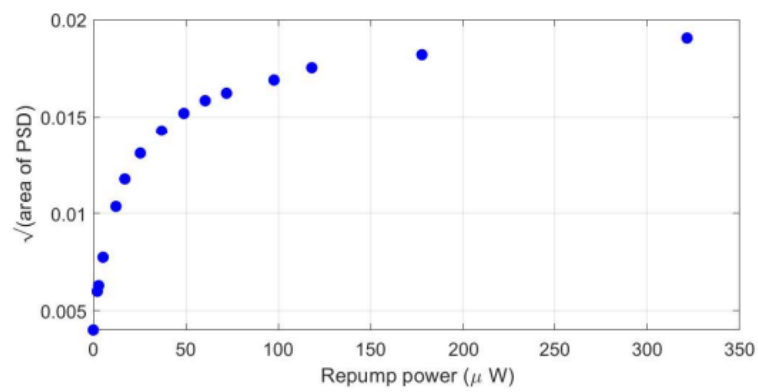
Figure A.5.: The square root of the area under the PSD as a function of the repump power

Bibliography B

[1]   I.M. Savukov, S.J. Seltzer, and M.V. Romalis. „Detection of NMR signals with a radio-frequency atomic magnetometer". In: *Journal of Magnetic Resonance* 185.2 (2007), pp. 214–220.

[2]   W. Wasilewski, K. Jensen, H. Krauter, J. J. Renema, M. V. Balabas, and E. S. Polzik. „Quantum Noise Limited and Entanglement-Assisted Magnetometry". In: *Phys. Rev. Lett.* 104 (13 Mar. 2010), p. 133601.

[3]   Andrei Derevianko and Hidetoshi Katori. „Colloquium: Physics of optical lattice clocks". In: *Rev. Mod. Phys.* 83 (2 May 2011), pp. 331–347.

[4]   D. J. Wineland, J. J. Bollinger, W. M. Itano, and D. J. Heinzen. „Squeezed atomic states and projection noise in spectroscopy". In: *Phys. Rev. A* 50 (1 July 1994), pp. 67–88.

[5]   Marco Schioppo, Roger Brown, William McGrew, *et al.* „Ultra-stable optical clock with two cold-atom ensembles". In: *Nature Photonics* 11 (July 2016).

[6]   F. Ya. Khalili and E. S. Polzik. „Overcoming the Standard Quantum Limit in Gravitational Wave Detectors Using Spin Systems with a Negative Effective Mass". In: *Phys. Rev. Lett.* 121 (3 July 2018), p. 031101.

[7]   M e Tse, Haocun Yu, Nutsinee Kijbunchoo, A Fernandez-Galiana, P Dupej, L Barsotti, CD Blair, DD Brown, SE Dwyer, A Effler, *et al.* „Quantum-Enhanced Advanced LIGO Detectors in the Era of Gravitational-Wave Astronomy". In: *Phys. Rev. Lett.* 123 (23 Dec. 2019), p. 231107.

[8]   Fausto Acernese, M Agathos, L Aiello, A Allocca, A Amato, S Ansoldi, S Antier, M Arène, N Arnaud, S Ascenzi, *et al.* „Increasing the Astrophysical Reach of the Advanced Virgo Detector via the Application of Squeezed Vacuum States of Light". In: *Phys. Rev. Lett.* 123 (23 Dec. 2019), p. 231108.

[9] H. Grote, K. Danzmann, K. L. Dooley, R. Schnabel, J. Slutsky, and H. Vahlbruch. „First Long-Term Application of Squeezed States of Light in a Gravitational-Wave Observatory". In: *Phys. Rev. Lett.* 110 (18 May 2013), p. 181101.

[10] Dmitry Budker and Michael Romalis. „Optical magnetometry". In: *Nature Physics* 3.4 (Apr. 2007), pp. 227–234.

[11] Arne Wickenbrock, Nathan Leefer, John W. Blanchard, and Dmitry Budker. „Eddy current imaging with an atomic radio-frequency magnetometer". In: *Applied Physics Letters* 108.18 (2016), p. 183507. eprint: `https://doi.org/10.1063/1.4948534`.

[12] H. Xia, Andrei Ben-Amar Baranga, D. Hoffman, and Michael Romalis. „Magnetoencephalography with an atomic magnetometer". In: *Applied Physics Letters - APPL PHYS LETT* 89 (Nov. 2006).

[13] Elena Boto, Sofie S. Meyer, Vishal Shah, *et al.* „A new generation of magnetoencephalography: Room temperature measurements using optically-pumped magnetometers". In: *NeuroImage* 149 (2017), pp. 404–414.

[14] G. Bison, N. Castagna, A. Hofer, P. Knowles, J.-L. Schenker, M. Kasprzak, H. Saudan, and A. Weis. „A room temperature 19-channel magnetic field mapping device for cardiac signals". In: *Applied Physics Letters* 95.17 (Oct. 2009), p. 173701.

[15] Kasper Jensen, Rima Budvytyte, Rodrigo Thomas, *et al.* „Non-invasive detection of animal nerve impulses with an atomic magnetometer operating near quantum limited sensitivity". In: *Scientific Reports* 6 (Jan. 2016).

[16] Luca Marmugi and Ferruccio Renzoni. „Optical Magnetic Induction Tomography of the Heart". In: *Scientific Reports* 6 (Apr. 2016), p. 23962.

[17] Natalia A Trayanova, Dan M Popescu, and Julie K Shade. „Machine learning in arrhythmia and electrophysiology". In: *Circulation Research* 128.4 (2021), pp. 544–566.

[18] W. Zheng, H. Wang, R. Schmieg, A. Oesterle, and E. S. Polzik. *Quantum enhanced electromagnetic induction measurement with an atomic magnetometer*. Manuscript in preparation, University of Copenhagen. 2022.

[19] Isaac Roca Caritg. „Experimental implementation of a Top Hat beam shaper". MA thesis. University of Copenhagen, 2022.

[20] Brian Julsgaard. „Entanglement and Quantum Interactions with Macroscopic Gas Samples". PhD thesis. University of Aarhus, 2003.

[21] Heng Shen. „Spin squeezing and entanglement with room temperature atoms for quantum sensing and communication". PhD thesis. University of Copenhagen, 2014.

[22] Hanna Krauter. „Generation and application of entanglement of room temperature ensembles of atoms". PhD thesis. University of Copenhagen, 2011.

[23] Kasper Jensen. „Quantum Information Entanglement and Magnetometry with Macroscopic Gas Samples and Non-Classical Light". PhD thesis. University of Copenhagen, 2011.

[24] Jens Arnbak. „Magnetocardiography and Eddy-Current Imaging using an Optical Cesium Vapor Magnetometer". MA thesis. University of Copenhagen, 2018.

[25] Eric D. Black. „An introduction to Pound–Drever–Hall laser frequency stabilization". In: *American Journal of Physics* 69.1 (2001), pp. 79–87.

[26] Scott Seltzer. „Developments in alkali-metal atomic magnetometry". In: (Jan. 2008).

[27] Kasper Jensen, Michael Zugenmaier, Jens Arnbak, Hans Stærkind, Mikhail V. Balabas, and Eugene S. Polzik. „Detection of low-conductivity objects using eddy current measurements with an optical magnetometer". In: *Phys. Rev. Research* 1 (3 Nov. 2019), p. 033087.

[28] Ryan Yde. „Room temperature spin ensembles for precision measurements". MA thesis. University of Copenhagen, 2020.

[29] Rebecca Schmieg. „Observation of non-classical photon pairs from room-temperature atomic ensembles through suppression of four wave mixing and classical noise sources". MA thesis. University of Copenhagen, 2019.

[30] G. Vasilakis, H. Shen, K. Jensen, M. Balabas, D. Salart, B. Chen, and E. S. Polzik. „Generation of a squeezed state of an oscillator by stroboscopic back-action-evading measurement". In: *Nature Physics* 11 (2015), pp. 389–392.

[31] Dmitry Budker and Derek F. Jackson Kimball. *Optical Magnetometry*. Cambridge University Press, 2013.

[32] Antti J. Mäkinen, Rasmus Zetter, Joonas Iivanainen, Koos C. J. Zeven-hoven, Lauri Parkkonen, and Risto J. Ilmoniemi. „Magnetic-field model-ing with surface currents. Part I. Physical and computational principles of bfieldtools". In: *Journal of Applied Physics* 128.6 (2020), p. 063906. eprint: `https://doi.org/10.1063/5.0016090`.

[33] Rasmus Zetter, Antti J. Mäkinen, Joonas Iivanainen, Koos C. J. Zeven-hoven, Risto J. Ilmoniemi, and Lauri Parkkonen. „Magnetic field model-ing with surface currents. Part II. Implementation and usage of bfield-tools". In: *Journal of Applied Physics* 128.6 (2020), p. 063905. eprint: `https://doi.org/10.1063/5.0016087`.

[34] C. V. Dodd and W. E. Deeds. „Analytical Solutions to Eddy-Current Probe-Coil Problems". In: *Journal of Applied Physics* 39.6 (1968), pp. 2829–2838. eprint: `https://doi.org/10.1063/1.1656680`.

[35] Koos C. J. Zevenhoven, Sarah Busch, Michael Hatridge, Fredrik Öisjöen, Risto J. Ilmoniemi, and John Clarke. „Conductive shield for ultra-low-field magnetic resonance imaging: Theory and measurements of eddy currents". In: *Journal of Applied Physics* 115.10 (2014), p. 103902. eprint: `https://doi.org/10.1063/1.4867220`.

[36] Hans Chr. Stærkind. *Magnetic Bias-Field Coil Design and Characterization*. Bachelor's Thesis, University of Copenhagen. 2015.

[37] Rebecca Schmieg. *Coherent dynamics of atomic vapors*. Project report, University of Copenhagen. 2018.